MAGNETO-HYDRODYNAMIC INSTABILITIES IN JETS : DYNAMICAL AND EMISSION PROPERTIES

M.Sc. Thesis

By:
Nikhil Borse

DISCIPLINE OF ASTRONOMY , ASTROPHYSICS AND SPACE ENGINEERING

INDIAN INSTITUTE OF TECHNOLOGY INDORE

June, 2020

MAGNETO-HYDRODYNAMIC INSTABILITIES IN JETS : DYNAMICAL AND EMISSION PROPERTIES

A THESIS

Submitted in partial fulfillment of the requirements for the award of the degree

of

Master of Science

by

NIKHIL BORSE

DISCIPLINE OF ASTRONOMY , ASTROPHYSICS AND SPACE ENGINEERING

INDIAN INSTITUTE OF TECHNOLOGY INDORE

June, 2020

INDIAN INSTITUTE OF TECHNOLOGY INDORE

CANDIDATE'S DECLARATION

I hereby certify that the work which is being presented in the thesis entitled **Magneto-hydrodynamic Instabilities in Jets : Dynamical and Emission Properties** in the partial fulfillment of the requirements for the award of the degree of **MASTER OF SCIENCE** and submitted in the **DISCIPLINE OF ASTRONOMY, ASTROPHYSICS AND SPACE ENGINEERING, Indian Institute of Technology Indore**, is an authentic record of my own work carried out during the time period from July, 2019 to June, 2020 under the supervision of Dr. Bhargav Vaidya.

The matter presented in this thesis has not been submitted by me for the award of any other degree of this or any other institute.

23/06/2020

Signature of the student with date
(NIKHIL BORSE)

This is to certify that the above statement made by the candidate is correct to the best of my/our knowledge.

23/06/2020

Signature of the Supervisor of
M.Sc. thesis #1 (with date)
(DR. BHARGAV VAIDYA)

Nikhil Borse has successfully given his/her M.Sc. Oral Examination held on **15th June, 2020.**

Suman Majumdar

Signature of Supervisor of MSc thesis
Date: 23/06/2020

Convener, DPGC
Date: 24/06/2020

Suman Majumdar

Signature of PSPC Member #1
Date: 24/06/2020

Signature of PSPC Member #2
Date: June 24, 2020

Abstract

The effect of MHD instabilities on the non-thermal continuum emission spectra and dynamics of kilo-parsec scale jets is being investigated. The dynamical evolution of a cylindrical jet configuration with a helical magnetic field and a radially sheared axial flow has been studied using non-relativistic three-dimensional numerical simulations. The helical magnetic field makes the jet prone to kink instabilities whereas the case with a uniform magnetic field exhibits Kelvin Helmholtz instability on account of MHD turbulence. The kink instabilities suppress vortex growth at the jet surface by enhancing the azimuthal magnetic field which has a stabilizing effect on the jet. We have developed a simplistic prescription of emission modeling to study the effects of instabilities on the jet emission - the multi-zone model. The results in a limiting case of this model- a " One-zone model" have been validated using an open-source package, the NAIMA code. The radiative models include synchrotron and inverse-Compton emission. Multi-zone SED modeling has been carried out for the synchrotron component alone for accurate modeling of the continuum spectra assuming a power-law distribution of relativistic cosmic-ray electrons and a line of sight inclined at two different viewing angles with the jet axis. The total integrated flux levels for the jet with a helical magnetic field are higher as compared to the one with a uniform axial field due to the additional azimuthal magnetic field. The difference between the two drops with increasing values of the line of sight inclination θ. As the multi-zone model fails to capture localized physical effects such as shocks and particle acceleration, a hybrid macro-particle based model has been used for more accurate emission modeling. The effect of jet velocity on the emission has been studied for the helical and uniform magnetic field cases by comparing the results from both the multi-zone and the hybrid macro-particle based models for three different magnitudes of the jet velocity on-axis. If the Kelvin-Helmholtz instability dominates, it disrupts the flow causing shock formation which results in a flatter emission spectrum whereas the interaction between the kink and Kelvin-Helmholtz instabilities has a stablilizing effect on the jet making the emission spectra steep. Having studied the effects of MHD instabilities on the jet emission, our future investigations will focus on the polarization aspect of the jet emission to probe into the magnetic field structure.

Contents

List of Figures

List of Tables

Chapter 1

Introduction

An astrophysical plasma column or jet is, by definition, an enormous collimated outflow of quasi-neutral ionized gas ejected along the rotational axis of the energy source or “central engine” which powers it. Radio observations of these jets reveal length scales ranging from a few parsecs to the order of mega-parsecs or in other words from stellar sizes to galactic proportions. In terms of the Schwarzschild radii of the central engine, these range from r_s to $10^9 r_s$. The emission that we observe from astrophysical jets is non-thermal and comes primarily from ultra-relativistic free electrons in the quasi-neutral plasma and ranges from low photon energies in radio up to high energies in the γ-ray band of the electromagnetic spectrum. There is a wide variety of astrophysical sources of jets such as young stellar objects or YSOs, micro-quasars and, pulsars that emit jets at parsec scales while Active Galactic Nuclei are responsible for what is known as AGN jets at scales of the order of one astronomical unit to mega-parsecs. The stellar size jets are powered by neutron stars or stellar-mass black holes whereas the central engine of AGN jets is a super-massive black hole. Astrophysical jets are a commonly occurring phenomenon in the universe. The jets in which the bulk flow accelerates up to relativistic speeds with Lorentz factors of the order of 10 or greater in proximity to the black hole are known as relativistic jets as they exhibit relativistic effects whereas AGN jets at the kilo-parsec scales having Lorentz factors of the order of 1 to 1.5 are treated as non-relativistic which is the regime that the entirety of this work deals with. These jets play a vital role in angular momentum and energy transport from the accretion disk to large distances from the central engine thereby heating the interstellar or intergalactic medium through turbulent interaction. They carry away a large fraction of the energy which comes from the accretion process. This transportation of angular momentum allows for the further accretion of matter onto the central engine. However, it is not yet clearly known what the jet matter is comprised of.

1.1 Instabilities in jets

The dominant mechanism by which AGN jets emit non-thermal radiation is synchrotron emission and this is evidenced from polarisation signatures in radio and optical observations of AGN jets. If the emission is highly polarized in radio through the optical frequency range, one can infer the presence of synchrotron emission and from the degree of polarization, the three-dimensional magnetic field structure can be probed. Thus, understanding the magnetic field structure of AGN jets using polarimetric data can tell us if the jet is stable or if there are any turbulent interactions and entrainment of ambient matter at the jet boundary. This kind of turbulent interaction is observed in AGN jets at large scales. This leads to the development of *Kelvin Helmholtz Instability* (hereafter KHI) at the jet boundary as there is a radial shear in the axial velocity of the bulk flow in the jet [11]. This is because the Kelvin Helmholtz instability is a pressure-driven hydrodynamic instability that develops at the interface between two fluids if there is a velocity gradient at the interface which is subjected to velocity perturbations. The KHI is illustrated in Fig. 2.1. The Kelvin Helmholtz instability, as it is pressure-driven, can also lead to the formation of shocks in the jet.

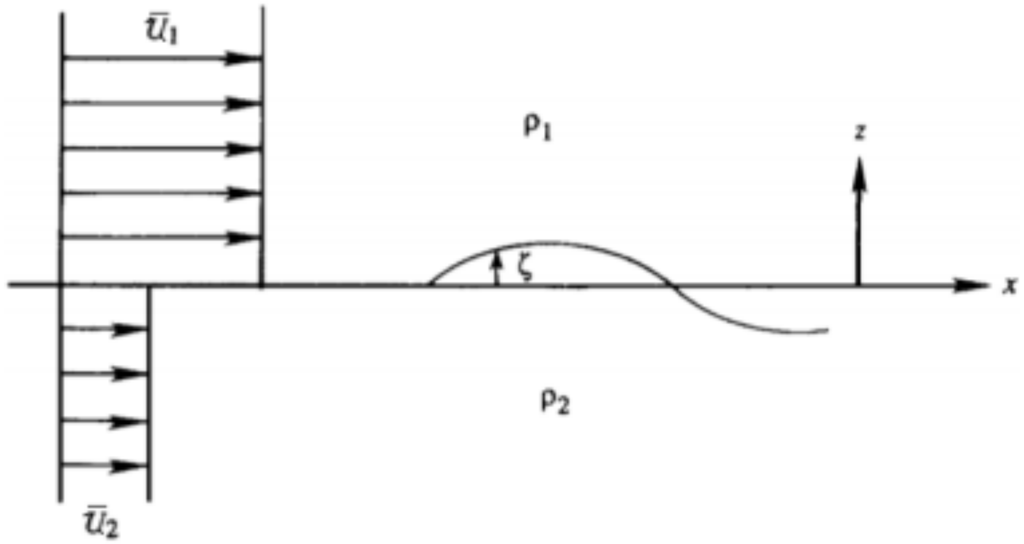

Figure 1.1: Kelvin Helmholtz Instability [10]

The magnetic field structure in AGN jets disentangled from the polarimetric observations can also reveal the current density distribution in the jet which when subjected to a kinked type of velocity perturbation leads to the development of kink instability in the core of the jet. The strength of the kink instability depends on the radial distribution of current density in the jet. The kink instability is illustrated in Fig. 4.1.

Therefore, it is safe to say based on observational evidence that the jet is bathed in a slew of instabilities and yet remains coherent over large scales. Why the jets remain stable over kilo-parsec to mega-parsec scales has been one of the long-standing questions in the physics of AGN jets.

At the base of the jet, close to the black hole, the energetics of the relativistic jet is magnetically dominated where the jet is subject to kink instabilities due to a non-zero current density parallel to the jet axis or due to the azimuthal magnetic field while at large scales away from the black hole, the jet is kinetically dominated and as a result of turbulent intermixing between the jet matter and the ambient medium at the jet boundary and the presence of a non-zero azimuthal magnetic field in the jet core, the result is that both KHI and Kink instabilities are observed at large scales. Three-dimensional non-relativistic dynamical simulations of a plasma column which replicates the magnetic field structure, velocity, density and pressure distribution of AGN jets at kilo-parsec scales have been performed to model the effect of Kink and KHI on the stability of the jet at large scales, its dynamical evolution and how the two instabilities interact with each other. To achieve this, a total of seven initial configurations having three different magnetic field structures are simulated. Two cases with different axial velocities have a

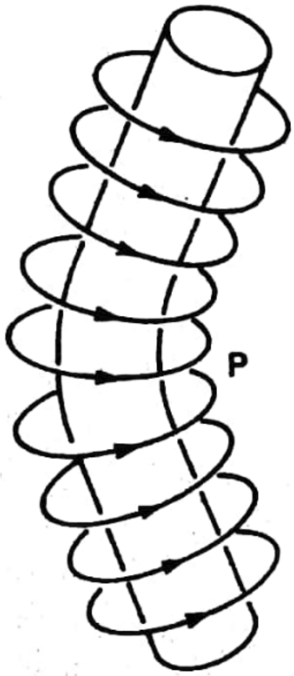

Figure 1.2: Kink Instability [10]

purely axial uniform magnetic field structure to simulate the purely hydrodynamic case of the KHI alone. All the other cases have a non-zero azimuthal magnetic field distribution such that both the KHI and kink instabilities develop simultaneously with KHI being the dominant instability in two of these configurations. The details of the simulation set-ups are provided in Chapter 2.

1.2 Motivation

The research goal is to study the effect of instabilities on the continuum emission spectra of AGN jets at large scales. We investigate whether the dominant type of instability can be inferred from the spectral signatures of the continuum emission from these jets. Another longstanding question being addressed is the stability or coherence of MHD jets at large scales despite the presence of both KHI and kink instabilities.

The thesis is structured in the following manner. Chapter 2 deals with dynamical simulation setups of astrophysical plasma columns with seven different initial conditions. Chapter 3 addresses our newly developed simplistic prescription of emission modeling-the multi-zone model by presenting results in a limiting case - a one-zone model, and validating the same to model the continuum emission spectra of the jet. The results for the dynamical and emission modeling are presented in Chapter 4 and their physical interpretation is discussed in Chapter 5 while a summary of these findings and the future outlook is given in the final chapter of the thesis.

Chapter 2

Numerical Setup

2.1 Equations and numerical methodology

The dynamical evolution of cylindrical plasma columns has been studied using numerical simulations that solve the following set of ideal time-dependent magneto-hydrodynamic equations in the Cartesian coordinate system.

$$\frac{\partial \rho}{\partial t} + \nabla.(\rho v) = 0 \tag{2.1}$$

$$\frac{\partial \rho v}{\partial t} + \nabla.\left(\rho v \otimes v - B \otimes B + \left(P + \frac{B.B}{2}\right) I\right) = 0 \tag{2.2}$$

$$\frac{\partial E}{\partial t} + \nabla.\left[\left(P + E + \frac{B^2}{2}\right) v - B(v.B)\right] = 0 \tag{2.3}$$

$$\frac{\partial B}{\partial t} + \nabla.[v \otimes B - B \otimes v] = 0 \tag{2.4}$$

$$\nabla.B = 0 \tag{2.5}$$

where ρ, B, and v are the density, local dynamic magnetic field, and velocity. The magnitude of B in code units is defined such that it is reduced by a factor of $\sqrt{4\pi}$ as compared to its physical counterpart. The energy density is the total of thermal, kinetic, and magnetic energy densities respectively. It is given by the following expression

$$E = \frac{P}{\Gamma - 1} + \frac{\rho v^2}{2} + \frac{B^2}{2} \tag{2.6}$$

where internal energy is governed by the ideal gas equation and the ratio of specific heats, Γ is 5/3. The following equation governs a scalar field which is used for tracking of fluid elements that were initially inside the jet radius. In other words, we set $\tau = 0$ for $R > R_j$ and $\tau = 1$ elsewhere.

$$\frac{\partial \rho \tau}{\partial t} + \nabla.(\rho \tau v) = 0 \tag{2.7}$$

During the initial phase of the simulation, ($t < 35$) the energy evolution equation can yield negative values for the pressure p due to truncation errors. So we switch to the following entropy evolution equation in those times for more accurate modeling.

$$\frac{\partial s}{\partial t} + v.\nabla(s) = 0 \tag{2.8}$$

where the entropy of the system is given by the expression

$$s = \frac{p}{\rho^{\Gamma}} \tag{2.9}$$

The numerical simulations are carried out employing the MHD module of the Astrophysical fluid dynamics code PLUTO [14]. A linear reconstruction shock-capturing method employing the hllc solver which is a Roe-type Riemann solver is used. This is accurate to the second order.

2.2 Initial conditions

The initial conditions for the jet models with the trans-sonic flow are chosen to be the same as given by Baty and Keppens [6]. The reference model with the trans-sonic flow ($M_s = 0.63$) on the jet axis, named as the UNI-A case has a uniform axial magnetic field. The other two models with the trans-sonic flow, HEL1-A, and HEL2-A are current-carrying magnetized jets with an initial helical magnetic field. In addition to these models, we investigate the dynamical evolution of three jet models with the supersonic flow ($M_s = 2.5$)on the jet axis, UNI-B, HEL1-B, HEL2-B, and one jet model with the hypersonic flow ($M_s = 5.0$) on the jet axis named as HEL2-C. The UNI-A and UNI-B cases are subject to purely hydro-dynamical KHI at the jet boundary while the HEL2-A, HEL2-B, and HEL2-C cases have a small pitch length relative to the jet radius making them more susceptible to the current-driven kink instabilities which can interact with the KH modes on the jet surface. The HEL1-A and HEL1-B cases have both instabilities with KHI being the dominant mode. This makes the HEL2-A, HEL2-B, and HEL2-C models particularly interesting to study the interaction between the two instabilities as that has implications for the jet stability at large scales.

The two fluids are assumed to have the same density with a thin shear layer relative to the jet radius at the boundary . The flow is along the axial direction and sheared radially with a hyperbolic tan profile. The initial radial distribution of the velocity field has the same form as chosen by Baty and Keppens [6]

$$V_z(r) = \frac{V}{2} \tanh\left(\frac{R_j - r}{a}\right) \tag{2.10}$$

where V is the amplitude of the velocity shear, R_j is the jet radius, a is the width of the shear layer and r is the radius in the cylindrical coordinate system. The values of these initial model parameters are $R_j = 1$, $a = 0.1$, on-axis pressure $p(r = 0) = p_0 = 1$, and a uniform density distribution with $\rho_0 = 1$ is chosen. The sonic speed on the jet axis is given by $(\gamma p_0/\rho_0)^{1/2} = 1.29$ as the ratio of specific heats is $\gamma = 5/3$. The flow regime of the jet can be found by calculating the Mach number along the axis using $M_s = V/2c_s$ which depends on the value of V that differs from case to case. The radial profile of the magnetic field structure for the seven cases can be expressed in the following general form given by Baty and Keppens [6]

$$B_r = 0, B_\phi = B_1 \frac{r/r_c}{1 + (r/r_c)^2}, B_z = B_0 \tag{2.11}$$

where the parameters B_0 and B_1 control the magnetic field strength and the radial pitch

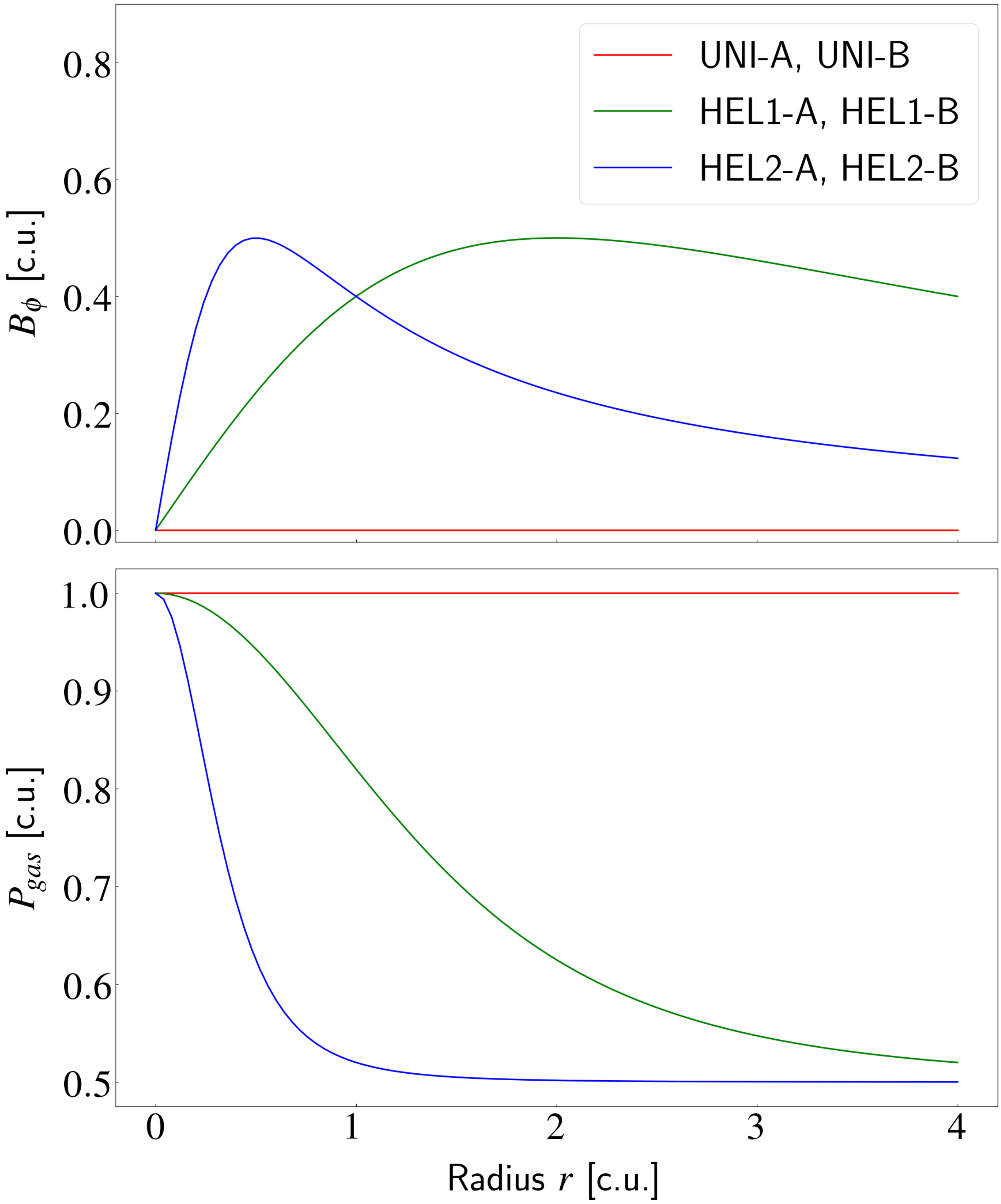

Figure 2.1: Initial radial profiles of B_ϕ, and gas pressure for all the jet models. The values are given in code units where 1 unit of magnetic field strength is 6.738 μG, 1 unit of pressure is $3.613 \times 10^{-12} dyne/cm^2$, and 1 unit of length is $100pc$.

profile and r_c is the characteristic column radius. For positive values of the parameter B_1, the current density has its maxima on the jet axis. The initial radial profiles of the azimuthal magnetic field B_ϕ are shown in Fig. 2.1. For the system to be in a state of magneto-hydrodynamic equilibrium initially, which is essentially a balance between gas pressure and magnetic pressure forces, the pressure distribution must follow the radial component of the momentum conservation equation which is given by

$$\nabla P = \frac{(\nabla \times B) \times B}{4\pi} \tag{2.12}$$

The radial profile of the pressure distribution can then be derived analytically from the radial component of the above expression to yield the form in equation 2.13 and is shown in Fig. 2.1 for all configurations.

$$P = P_0 - \frac{{B_1}^2}{2\rho_0}\left(1 - \frac{1}{[1+(r/r_c)^2]^2}\right) \tag{2.13}$$

An earlier work on kink instabilities assumed a constant pitch length for a force-free jet model [3]. In all our configurations given in Table 2.1, the radial pitch profile varies according to the following expression.

$$P_i = \frac{rB_z}{B_\phi} = \frac{r_c B_0}{B_1}\left[1 + \left(\frac{r}{r_c}\right)^2\right] \tag{2.14}$$

This is preferable to a uniform pitch profile for computational ease of numerical simulations. Also, a direct comparison can be made with the uniform axial magnetic field or UNI-A and UNI-B cases. As the toroidal magnetic field tends to zero at infinite distances, the current density in the jet must be counterbalanced by a reverse current flow in the jet ambient medium. The values of the model parameters B_1 and B_0 are 1 and 0.25 respectively. The toroidal component of the magnetic field is the same for HEL1-A, HEL1-B, HEL2-A, HEL2-B, and HEL2-C cases at the jet boundary. This facilitates comparisons between the respective trans-sonic and supersonic jet models by separating the effects of the localised magnetic field. A summary of the detailed model parameters for all the cases is given in Table 2.1.

Table 2.1: Summary of parameters in the initial configuration of the jet. Here, the magnetic pitch parameter P_i, sonic Mach number M_s, and axial velocity V_z are specified on the jet axis, B_z is the axial magnetic field, B_ϕ is the azimuthal magnetic field, and r_c is the characteristic column radius. All values are given in code units.

Case	r_c	P_i/R_j	M_s	V_z	B_z	$B_\phi(r=R_j)$
UNI-A	...	∞	0.63	0.81	0.25	0
HEL1-A	2	0.5	0.63	0.81	0.25	0.4
HEL2-A	0.5	0.125	0.63	0.81	0.25	0.4
UNI-B	...	∞	2.50	3.22	0.25	0
HEL1-B	2	0.5	2.50	3.22	0.25	0.4
HEL2-B	0.5	0.125	2.50	3.22	0.25	0.4
HEL2-C	0.5	0.125	5.00	6.45	0.25	0.4

Table 2.2: The relation between physical and code units

Quantity	Code unit	Physical unit
Length	1	$100pc = 3.086 \times 10^{20} cm$
Velocity	1	$600 km/s = 6 \times 10^{7} cm/s$
Time	1	$1.63 \times 10^{5} yr$
Magnetic field	1	$6.738 \times 10^{-6} G$
Density	1	$1.004 \times 10^{-27} g/cm^{3}$
Pressure	1	$3.613 \times 10^{-12} dyne/cm^{2}$

A periodic boundary condition is used along the axial direction which restricts the wavelength of the perturbations to values that fit within the length L_z, which is the size of the computational domain along the axial direction. The domain size is given by $4R_j \times 4R_j \times L_z$ where the aspect ratio $L_z/R_j = 2$. The boundary condition on the side walls is chosen as reflective or fixed to have a helical field structure in the jet. The boundaries do not interfere with the flow in the period of the simulations. The resolution of the grid is set to $200 \times 200 \times 100$ zones or $400 \times 400 \times 200$ parsecs in physical units. The simulations were carried out using 24 processors on the Sun grid engine computing cluster.

The magneto-hydrodynamic equilibrium is perturbed only using the $m = \pm 1$ KH modes which are thought to play a pivotal role in jet stability. The mathematical form of the velocity perturbations applied to the three cases is given by equation 2.15

$$v_r = \delta V \exp\left(-\frac{(r - R_j)^2}{16a^2}\right) \cos(m\theta) \sin\left(\frac{2\pi n z}{L_z}\right) \tag{2.15}$$

where $\delta V = 0.01$ is the amplitude of the applied velocity perturbation, $4a = 0.2$ is its width along the radial direction. The axial and azimuthal numbers are set to $n = 1$ and $m = 1$ to excite the Fourier modes that may play a role in stabilizing the jet. These can easily trigger KH modes on the surface and kink modes in the presence of non zero current density as there is a small yet finite displacement of the jet localized at the boundary or the jet radius R_j.

The relation between physical and code units is given in Table 2.2. The simulation runs for trans-sonic jet models UNI-A, HEL1-A and HEL2-A were stopped at $t = 15.0$ in code units while the runs for corresponding supersonic jet models UNI-B, HEL1-B, and HEL2-B were stopped at $t = 25.0$ as it takes a relatively long time for the instabilities to develop in these cases due to a higher sonic Mach number M_s along the jet axis.

Chapter 3

Emission Modelling

To study the effects of magneto-hydrodynamic instabilities on the continuum emission spectra of jets at large scales, we have developed a post-processing tool for modeling the non-thermal emission. By modeling the emission, we obtain intensity maps at any desired time instant. The emission processes described in the following sections 3.1 and 3.2 are synchrotron and IC emission respectively.

3.1 Synchrotron emission

The synchrotron emission from jets occurs mainly due to ultra-relativistic particles. We assume that these emitting particles are electrons and their energy distribution is a power-law with spectral index p. The total synchrotron emissivity per unit frequency is a function of observing frequency ν and the direction of our line of sight $\hat{n}_{los}$. Given the synchrotron power radiated by a single electron $P(\nu, \gamma)$, the total synchrotron emissivity due to an ensemble of ultra-relativistic electrons is computed by integrating the following expression given by Vaidya et al. [23]

$$J_{syn}(\nu, \hat{n}_{los}) = \int P(\nu, \gamma) N(\gamma) d\gamma \tag{3.1}$$

where $N(\gamma)d\gamma$ is the total number of electrons per unit volume having a Lorentz factor in the range γ to $\gamma + d\gamma$.
It can also be expressed in the form given by Pandya et al. [15] and Reissl et al. [18]

$$J_{syn}(\nu, \hat{n}_{los}) = \frac{\nu_c (p-1) 3^{p/2}}{\gamma_{min}^{1-p} - \gamma_{max}^{1-p}} \left(\frac{\nu}{\nu_c sin\theta} \right)^{\frac{1-p}{2}} \frac{n_e^{NT} e^2}{c 2^{\frac{p+1}{2}}} \int_{x_1}^{x_2} F(x) x^{\frac{p-3}{2}} dx \tag{3.2}$$

where ν_c is the critical frequency of synchrotron emission for a single electron, θ is the angle between the line of sight vector $\hat{n}_{los}$ and the magnetic field vector $\vec{B}$, n_e^{NT} is the number density of non-thermal electrons, and $F(x)$ is the synchrotron function that is the modified Bessel function integral of the order 5/3

$$F(x) = x \int_x^\infty K_{5/3}(\eta) d\eta \tag{3.3}$$

where $x = \frac{\nu}{\nu_c}$

3.2 IC emission

The same electron population which is responsible for the synchrotron emission from jets scatters microwave seed photons from the Cosmic Microwave Background in jets at kpc-scales resulting in inverse-Compton or IC emission - the IC/CMB model which has been described by Breiding et al. [9]. We assume an isotropic seed photon distribution and the bulk-flow of the jet at kpc-scales to be in the non-relativistic limit. The total IC emissivity at a particular frequency due to this ensemble of ultra-relativistic electrons can be computed using the form given by Petruk [16]

$$J_{IC}(\nu) = \int p(\nu,\gamma) N(\gamma) d\gamma \tag{3.4}$$

It can also be expressed in the form given by Blumenthal and Gould [7]

$$J_{IC}(\nu) = \frac{3ch\sigma_T n_e^{NT}(p-1)2^{p-2}}{4\pi\left(\gamma_{min}^{1-p} - \gamma_{max}^{1-p}\right)\nu^{\frac{p-1}{2}}} \int d\nu_1\, \nu_1^{\frac{p-3}{2}} \epsilon(\nu_1) \int_{x_1}^{x_2} dx\, x^{\frac{p-1}{2}} f(x) \tag{3.5}$$

where σ_T is the Thomson scattering cross-section, and $\epsilon(\nu_1)$ is the black-body distribution of the seed photons from the Cosmic Microwave Background given by the expression,

$$\epsilon(\nu_1) = \frac{8\pi h}{c^3} \frac{\nu_1^3}{\exp\left(h\nu_1/KT_{CMB}\right) - 1} \tag{3.6}$$

As the electron energy γ in our setups ranges well below the critical klein-Nishina Lorentz factor γ_k which equals $\frac{0.53 m_e c^2}{K_B T} = 10^9$ according to Schlickeiser and Ruppel [20], and Petruk[16] for a CMB photon with $T_{CMB} = 2.73K$, the losses due to IC emission will be in the Thomson limit and the function $f(x)$ is then given by

$$f(x) = 2x\ln(x) + 1 + x - 2x^2, \qquad 0 \;<\; x \;<\; 1 \tag{3.7}$$

where $x = \frac{\nu}{4\gamma^2\nu_1}$

3.3 One-zone model

Our one-zone model assumes that the emitting region is a homogeneous spherical blob [19] and it moves along the jet axis at a non-relativistic velocity at large scales. As a result, we do not see any beaming effects and the Doppler boosting factor $\delta \to 1$ for all viewing directions. The unit vector along the line of sight $\hat{n}_{los}$ is specified by the spherical co-ordinates θ and ϕ in which we fix the value of ϕ to $0°$. We assume that the magnetic field is uniform in the emitting region with the magnetic field strength B. The radius of the blob is set to the order of the jet radius $R_j = 100pc$. The distance between the blob and the observer is defined as D.

The energy distribution of the emitting ultra-relativistic electrons is assumed to be a power-law with spectral index p given by

$$N(\gamma)d\gamma = N_0\gamma^{-p}d\gamma, \qquad \gamma_{min} \;<\; \gamma \;<\; \gamma_{max} \tag{3.8}$$

where γ_{min} and γ_{max} are the limits of the electron energies and N_0 is the normalization constant. The ratio of the number density of the non-thermal electrons to the total

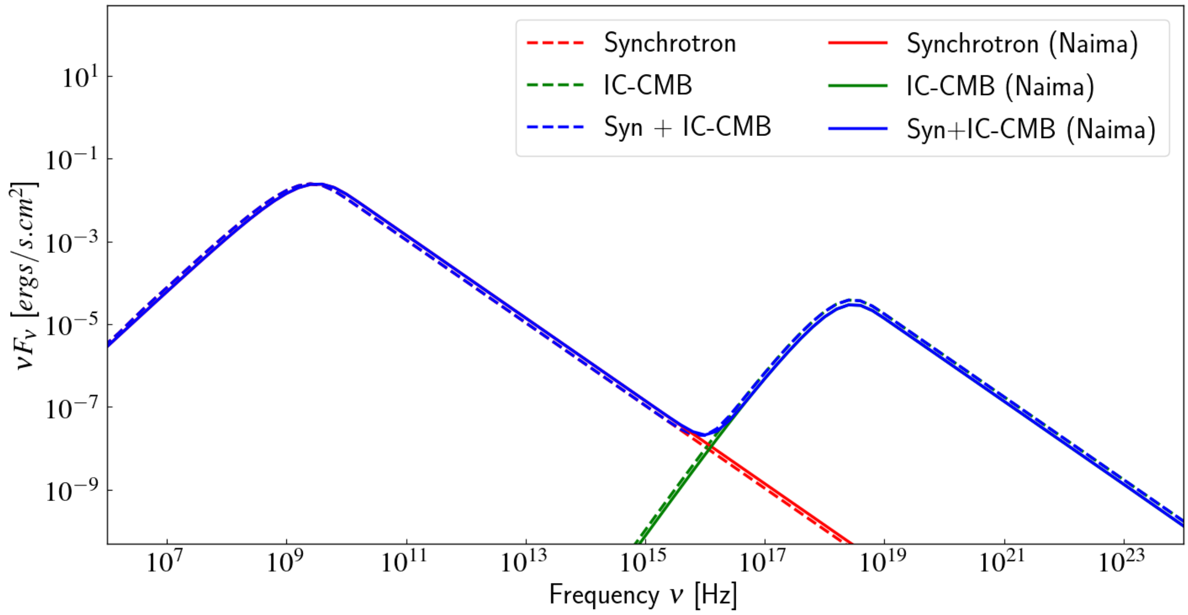

Figure 3.1: Comparison between SED of synchrotron and inverse-Compton emission from power-law distribution of emitting electrons in the jet with spectral index, p = 5 obtained using NAIMA and one-zone model keeping all other model parameters the same.

number density of the jet plasma is defined as the parameter η^{NT}. One of the limitations of our one-zone model is that it has many parametric dependencies. The free parameters are $\eta^{NT}, p, \gamma_{min}, \gamma_{max}, \theta, B, R_j$, and D.

The total synchrotron and inverse-Compton emissivities can then be computed after assigning a certain set of values to these free parameters using equations 3.2 and 3.5 respectively.

3.4 Validation with one-zone model

We assigned a particular set of free parameters to model the synchrotron and IC emission from the jet at kpc-scales using our one-zone model. The parameters are minimum electron energy $E_0 = 1TeV$, power-law index $p = 5$, the distance between the blob and observer $D = 1.5kpc$, magnetic field strength $B = 100\mu G$, and the fraction representing non-thermal electron number density $\eta^{NT} = 0.01$. We then modeled the emission spectra using an open-source python package NAIMA [24] keeping all model parameters the same. A comparison of our results obtained using the one-zone model with those produced using the NAIMA code is shown in Fig. 3.1. While the NAIMA code uses analytical approximations for computing both the synchrotron [1] and IC [12] emissivities, our one-zone model computes the exact integrals in equations 3.2 and 3.5 numerically for more accurate results. Our results obtained using the one-zone model shown in Fig. 3.1 are in agreement with those produced using NAIMA across the electromagnetic spectrum ranging from frequencies between 1MHz in the radio waveband to 1YHz in the γ-ray band.

For all its simplicity and computational advantages, the one-zone model has its drawbacks. It has many parametric dependencies and assumptions regarding the geometry of the emitting region and the magnetic field structure. To overcome these shortcomings, we use a multi-zone emission model which is described in the next section.

3.5 Multi-zone model

The magnetic field and mass density structure in jets at large scales are spatially inhomogeneous which the one-zone model fails to capture. To accurately model the non-thermal continuum emission spectra of AGN jets at large scales, we use a simplistic prescription for emission modeling - the multi-zone model. In this approach, every grid cell of the computational domain is treated as a single zone for which the emissivity is modeled independently using equation 3.2 for the synchrotron and equation 3.5 for the IC/CMB radiative models respectively. Thus depending on the mass density and magnetic field structure, we can model a grid distribution of the emissivities $J_{syn}(\nu, \hat{n}_{los}, \mathbf{r})$ and $J_{IC}(\nu, \hat{n}_{los}, \mathbf{r})$ that depend on the position $\mathbf{r}$.

3.5.1 Generating Intensity Maps

To calculate the total flux density from the jet emission, the specific intensity distribution of the incident radiation in the sky plane must be mapped first. To calculate specific intensity $I_\nu(\nu, X, Y)$ of synchrotron emission at a particular frequency ν, we integrate the emissivity $J_{syn}(\nu, \mathbf{r})$ for a given line of sight along the direction $\hat{n}_{los}$ using the solution to the fundamental radiative transfer equation in the optically thin limit [23] which is given by

$$I_\nu(\nu, X, Y) = \int_{-\infty}^{\infty} J_{syn}(\nu, X, Y, Z) dZ \tag{3.9}$$

where we choose a Cartesian coordinate system with the Z-axis along the line of sight of the observer while the other two axes are in the sky plane. The ray-tracing geometry is shown in Fig. 7 of Porth et al. [17]. The same method is used for generating IC intensity maps as well.

3.5.2 Computing Flux Density

The flux density at a particular frequency ν can be estimated by integrating the specific intensity distribution over the solid angle subtended at the observer's position by the projection of the emitting region in the jet on the sky plane. This is given by

$$F_\nu(\nu) = \int I_\nu(\nu, X, Y) d\Omega \tag{3.10}$$

where the solid angle is given by $d\Omega = (dX \times dY)/D^2$. This equates to 6.47×10^{-14} steradians for an observer to source distance $D = 7.86$ Mpc corresponding to a redshift of $z = 0.00183$ for the blazar Centaurus A [22]. This is the distance D that we have used for modeling the emission from all the jet configurations. The dimensions of a grid zone are $dX = dY = dZ = 2pc$ and they depend on the chosen grid resolution. The total integrated flux density $F_\nu(\nu)$ can then be used to plot the continuum emission spectra. The same method is applied for plotting both the synchrotron and IC/CMB components of the SED.

3.6 Hybrid Macro-particle based model

One of the limitations of the multi-zone model which makes it a rather simplistic prescription for emission modeling is the assumption that the power-law distribution of relativistic electrons is spatially homogeneous. In order to take into account the effects of localized phenomena such as shocks or particle acceleration on the grid distribution of emissivities $J_{syn}(\nu, \hat{n}_{los}, \mathbf{r})$ and $J_{IC}(\nu, \hat{n}_{los}, \mathbf{r})$, we use the hybrid macro-particle based framework in the PLUTO code [23]. These localized effects influence the temporal evolution of the energy spectrum of the ultra-relativistic electrons. The hybrid framework in PLUTO allows for more accurate modeling of the non-thermal continuum emission spectra of AGN jets at kpc-scales. It follows a Lagrangian macro-particle based approach where each of these macro-particles has an ensemble of non-thermal particles attached to it. The detailed methodology of the hybrid macro-particle based model is given by Vaidya et al. [23]. We initialize all the runs listed in Table 2.1 using the hybrid framework in the PLUTO code with 600,000 Lagrangian macro-particles that are randomly distributed in the simulation box.

Chapter 4

Results

The methods of dynamical and emission modeling of magneto-hydrodynamic instabilities in jets have been described in Chapters 2 and 3 respectively. We describe the results obtained using dynamical modeling in the following section, while the results obtained from emission modeling will be described in sections 4.2 and 4.3.

4.1 Dynamical modeling results

We do the dynamical modeling of jets to study the effects of magneto-hydrodynamic instabilities on the jet dynamics and energetics. By solving the ideal MHD equations, we study the temporal evolution of three-dimensional scalar and vector fields such as mass density ρ, gas pressure P_{gas}, magnetic field $\vec{B}$, and velocity field $\vec{v}$. Three-dimensional snapshots of the jet density structure for the models UNI-A, UNI-B, HEL2-A, and HEL2-B at time $t = 15.0$ in code units is shown in Fig. 4.1. The jet boundary is perceptible in the snapshots of the models HEL2-A and HEL2-B. While the jet gets completely destroyed both the uniform magnetic field configurations, the respective helical configurations are relatively stable.

4.1.1 Jet energetics and validation of dynamical jet models

In order to validate our dynamical jet models, we set up our trans-sonic jet configurations with initial conditions identical to those given for the three configurations studied by Baty and Keppens [6]. For comparison, we plotted the time histories of the energies defined below for each configuration.

The volume-averaged kinetic energy confined to the x-y plane E^k_{xy} is given by

$$E^k_{xy} = \frac{1}{V_b} \int_{V_b} \frac{\rho V_x^2 + \rho V_y^2}{2} \, dx \, dy \, dz \tag{4.1}$$

and the volume-averaged perturbed magnetic energy confined to the x-y plane E^b_{xy}, is

$$E^b_{xy} = \frac{1}{V_b} \int_{V_b} \frac{B_x^2 + B_y^2}{2} \, dx \, dy \, dz - E^{b,0}_{xy} \tag{4.2}$$

where $V_b = 16 R_j^2 L_z$ is the simulation box volume and $E^{b,0}_{xy}$ is the initial magnetic energy obtained from the equilibrium conditions. The volume-averaged axial kinetic and perturbed magnetic energies are given by the following expressions

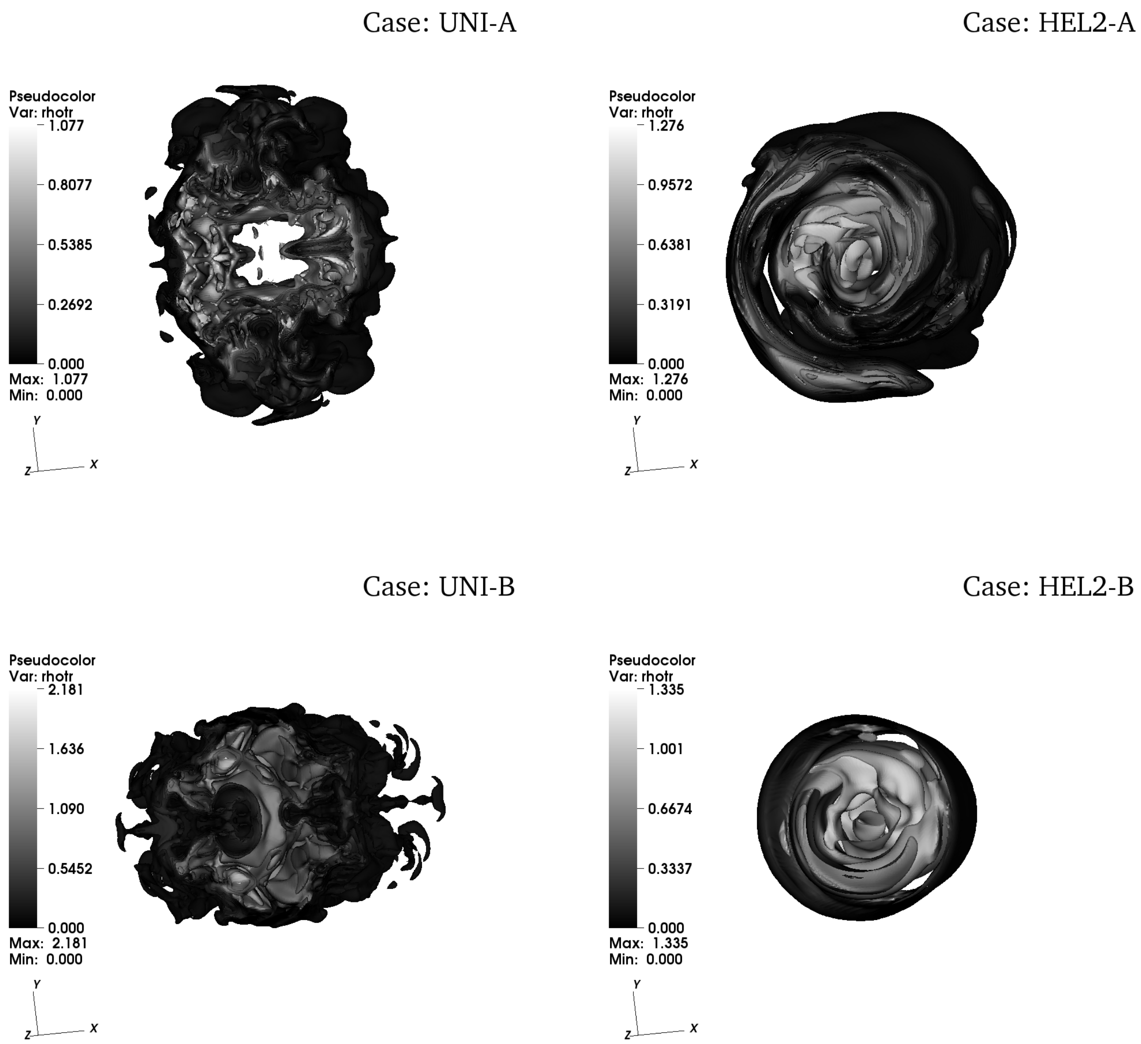

Figure 4.1: Top panels: The three-dimensional isosurface density contours of the model UNI-A (left-hand panel) and HEL2-A(right-hand panel) at time $t = 15.0$ in code units where 1 unit of time equals 1.63×10^5 years. Bottom panels: The corresponding density structure for models UNI-B and HEL2-B respectively at the same time.

$$E_z^k = \frac{1}{V_b} \int_{V_b} \frac{\rho V_z^2}{2} \, dx \, dy \, dz \tag{4.3}$$

$$E_z^b = \frac{1}{V_b} \int_{V_b} \frac{B_z^2}{2} \, dx \, dy \, dz - E_z^{b,0} \tag{4.4}$$

The results for all the jet configurations in Table 2.1 except HEL2-C is shown in Fig. 4.2. The results for the trans-sonic cases, UNI-A, HEL1-A, and HEL2-A shown in the left-hand panels of Fig. 4.2 are in agreement with those obtained by Baty and Keppens [6].

We extend this analysis to the supersonic jet configurations and the results are shown in the right-hand panels of Fig. 4.2. After a steady increase in energies E_{xy}^k and E_{xy}^b, they increase rapidly from times $t = 13.5$, and 10.5 in code units in the UNI-B and HEL2-B cases respectively. The axial kinetic energy E_z^k drops drastically at $t = 13.5$ in code units in the UNI-B case but no appreciable change is visible in the HEL2-B case at the same scale till the end of the run at $t = 25.0$. The axial perturbed magnetic energy first peaks at $t = 6.5$ and drops till $t = 13.5$ before increasing rapidly in the UNI-B case whereas in the HEL2-B case a sudden rise is seen from $t = 10.5$ in code units. In the HEL2-B case, all the energies become steady after $t = 14.0$ in code units following the phase in which they increase sharply.

4.2 Emission modeling results

We do the emission modeling of jets to study the effects of magneto-hydrodynamic instabilities on the continuum emission spectra of MHD jets. In order to study this, we apply the multi-zone model described in section 3.5 to obtain synchrotron emission maps for all the jet configurations at six different observing frequencies in the radio waveband at time $t = 9.0$ in code units for a direction along a line of sight inclined at $\theta = 10^\circ$ with the jet axis. The results for the UNI-A case are shown in Fig. 4.3. We assume that the energy distribution of the ultra-relativistic emitting electrons is a power-law with spectral index $p = 3$, and energy limits $\gamma_{min} = 100$ and $\gamma_{max} = 10^6$. The fraction of non-thermal electrons is taken as $\eta^{NT} = 10^{-3}$. The jet emission gets dimmer with an increase in observing frequency. A bright feature symmetric about the Y-axis resembling a figure of eight appears on either side of the jet boundary at all observing frequencies.

To study how the jet emission depends on the viewing direction $\hat{n}_{los}$, we apply the multi-zone model to obtain the SEDs of synchrotron emission for all the jet configurations when observing along two different lines of sight inclined at $\theta = 10^\circ$ and $\theta = 50^\circ$ respectively with the jet axis at time $t = 9.0$ in code units. The results are shown in Fig. 4.4. The total integrated flux levels in the UNI-A case are an order of magnitude lower than in the HEL1-A and HEL2-A cases for a direction along a line of sight that is close to the axial direction with $\theta = 10^\circ$. In their supersonic jet counterparts, this difference is enhanced to more than two orders of magnitude. For a direction along a line of sight that is inclined at $\theta = 50^\circ$ with the jet axis, the total integrated flux levels in all the jet configurations are of roughly the same order.

To improve the accuracy of our emission maps like the ones shown in Fig. 4.3, we use the hybrid framework in the PLUTO code for all the jet configurations. The results of the synchrotron emission maps obtained in the UNI-A case at time $t = 9.0$ in code units keeping all other initial model parameters the same are shown in Fig. 4.5. The

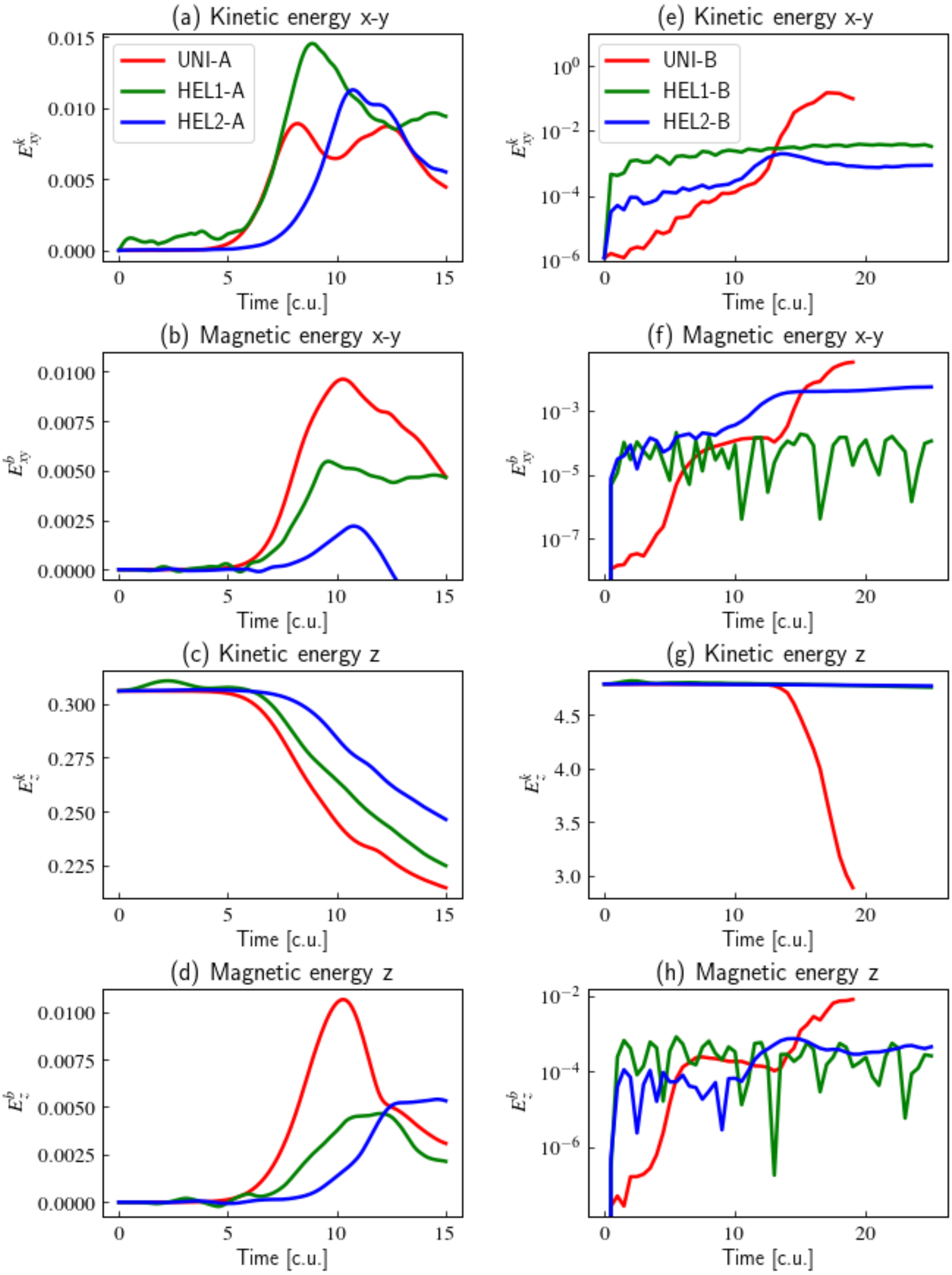

Figure 4.2: Left-hand panels: The time evolution of (a) the volume-averaged kinetic energy in the XY plane E^k_{xy}, (b) the volume-averaged perturbed magnetic energy in the XY plane E^b_{xy}, (c) the volume-averaged axial kinetic energy E^k_z, and (d) the volume-averaged axial perturbed magnetic energy E^b_z for all the trans-sonic jet models. Right-hand panels: The time evolution of corresponding energies for the supersonic jet model counterparts. The absolute values of perturbed magnetic energies are shown in panels (f) and (h).

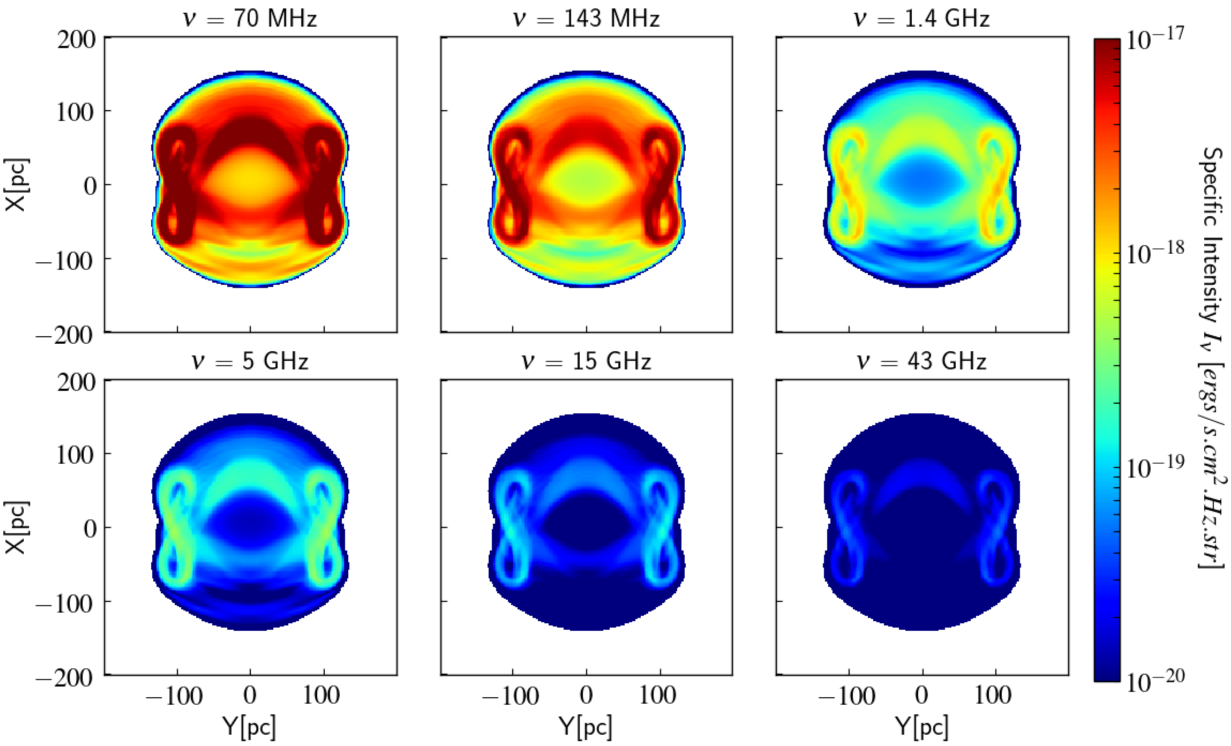

Figure 4.3: Synchrotron emission maps produced using the Multi-zone model for case UNI-A which has a trans-sonic flow at time t = 9.0 (in code units) with a power-law distribution of emitting electrons with spectral index, p=3 for a direction along a line of sight inclined at 10° with the jet axis at observing frequencies of (top panels) 70MHz, 143MHz, 1.4GHz,(bottom panels) 5GHz, 15GHz, and 43GHz. The colors represent the magnitude of specific intensity I_ν.

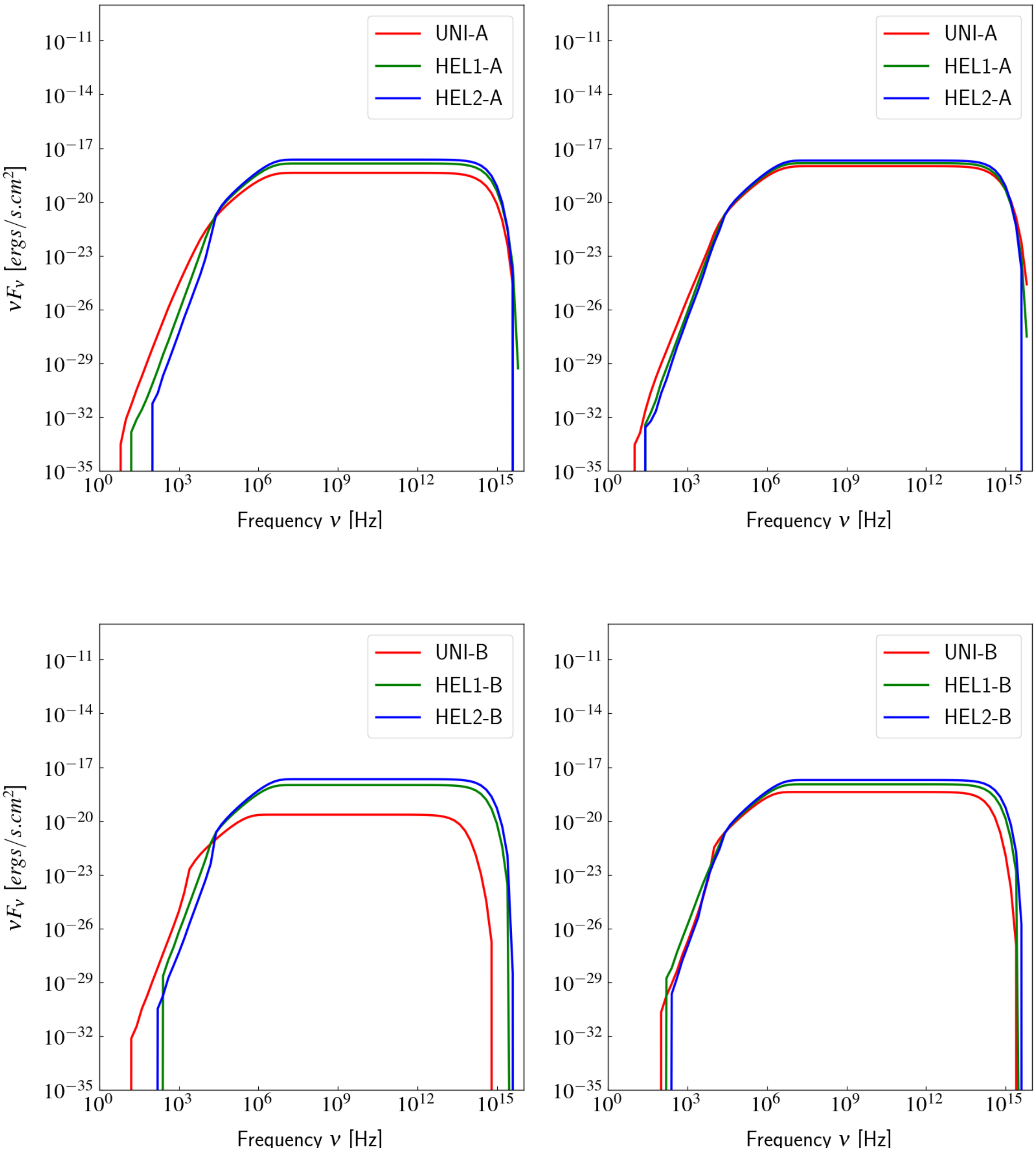

Figure 4.4: Top panels: The SED of synchrotron emission produced using the multi-zone model for the cases with the trans-sonic flow at time t = 9.0 (in code units) when seen from a direction inclined at 10° (left-hand panel) and 50° (right-hand panel) with the jet axis. Bottom panels: The corresponding results for the supersonic jet models keeping all other parameters the same.

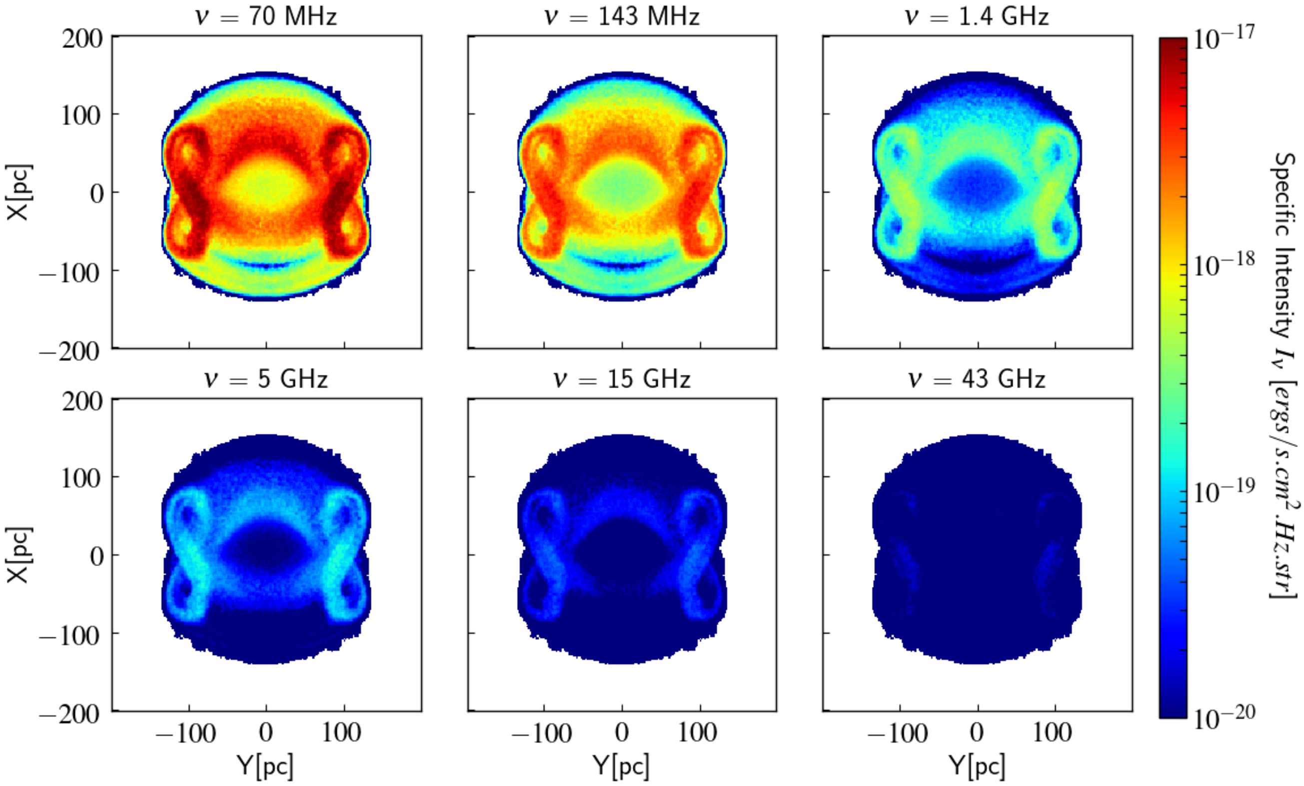

Figure 4.5: Synchrotron emission maps produced using the hybrid framework in the PLUTO code for case UNI-A at time t = 9.0 (in code units) with a power-law distribution of emitting electrons with spectral index, p=3 for a direction along a line of sight inclined at 10° with the jet axis at observing frequencies of (top panels) 70MHz, 143MHz, 1.4GHz,(bottom panels) 5GHz, 15GHz, and 43GHz.

jet emission gets dimmer with an increase in observing frequency as with the multi-zone model shown in Fig. 4.3. The bright feature resembling a figure of eight also appears just as in Fig. 4.3 at lower radio frequencies. However, as the observing frequency increases, we see an enhanced dimming in the jet emission. The bright feature almost vanishes in the emission map obtained using an observing frequency of $\nu = 43$GHz.

Using the hybrid framework in the PLUTO code, no shocks were captured in any of the trans-sonic jet models UNI-A, HEL1-A, or HEL2-A. We ramp up the initial sonic Mach number to $M_s = 2.5$ along the jet axis for all three configurations to study its effects on the jet emission. In the resulting supersonic jet models UNI-B, HEL1-B, and HEL2-B, we choose a spectral index $p = 6$ for the initial power-law distribution of non-thermal particles. We use the hybrid framework in the PLUTO code to obtain both synchrotron and inverse-Compton emission maps at three different energies for all three supersonic jet configurations at time $t = 15.0$ in code units for a direction along a line of sight inclined at $\theta = 20°$ with the jet axis. The observing frequencies for the synchrotron emission maps are 10MHz, 1GHz, and 100GHz in the radio waveband whereas the energies for the inverse-Compton emission maps are 40KeV, 4MeV and 400MeV in the γ-ray band. The results for the UNI-B case are shown in Fig. 4.6. The jet emission gets dimmer with increasing energies in both the synchrotron and inverse-Compton emission maps. A bright feature symmetric about the X-axis appears in the central region of the jet at all three energies.

4.3 SED modeling

In order to understand the effects of MHD instabilities on the jet emission, we study the temporal evolution of the continuum emission spectra of the jet for all the supersonic jet configurations and do a comparative analysis. The results for the UNI-B case obtained using the hybrid framework in the PLUTO code while keeping all model parameters the same are shown in Fig. 4.7. The synchrotron component of the SED is on the left-hand side of the plot while the inverse-Compton component is on the right-hand side. The total integrated flux represented by circles is calculated for 6 different frequencies uniformly distributed in log-space ranging from 10^7Hz to 10^{17}Hz for synchrotron emission and 10^{17}Hz to 10^{27}Hz for IC emission. The times at which the SED is plotted are $t = 0.0, 0.5, 1.0, 2.5, 4.5, 6.5, 9.0, 11.5, 13.5, 14.0, 14.5,$ and 15.0 in code units. The initial SED is a straight line given the power-law distribution of non-thermal electrons and is shown using a black-dashed line for both the components. This is steeper than the SED in Fig. 4.4 as the spectral index of the particle distribution has been increased to $p = 6$. The colors change from dark to bright with increasing times. For the synchrotron component, the total integrated flux at high frequencies of 10^{15}Hz in the optical waveband and 10^{17}Hz in the X-ray band drops progressively with time as is indicated by the SEDs at times $t = 0.5, 1.0, 2.5, 4.5, 6.5, 9.0,$ and 11.5. A sudden flattening of the SED occurs at time $t = 13.5$ as the total integrated flux at high frequencies of 10^{15}Hz and 10^{17}Hz jumps drastically. The total integrated flux levels at these frequencies keep increasing further with time as shown by the SEDs at times $t = 14.0, 14.5,$ and 15.0. The inverse-Compton component of the SED evolves similarly to its synchrotron counterpart.

To study the effect of MHD instabilities on the continuum emission spectra of jets, we compare the spectra of the uniform magnetic field configuration UNI-B with the helical magnetic field configurations HEL2-B and HEL2-C obtained using the hybrid framework in the PLUTO code. The comparison at time $t = 15.0$ in code units is shown in Fig. 4.8. The continuum emission spectra for the UNI-B, HEL2-C, and HEL2-B cases are represented by red, green, and blue dashed lines respectively. As in Fig. 4.7, the total integrated flux is calculated for 6 different frequencies each for the synchrotron emission represented by circles and IC emission represented by triangles. In the HEL2-B and HEL2-C cases, the total integrated flux for synchrotron emission drops sharply at frequencies of 10^{15}Hz in the optical waveband and 10^{17}Hz in the X-ray band whereas in the UNI-B case, after an initial decline of total integrated flux at lower energies, the synchrotron component of the SED flattens out at a frequency of 10^{13}Hz and the total integrated flux increases at higher frequencies of 10^{15}Hz and 10^{17}Hz. In the HEL2-C case, the total integrated flux for synchrotron emission is relatively increased as compared to the HEL2-B case at a frequency of 10^{17}Hz in the X-ray band while the flux levels are nearly identical for both cases at all the other observing frequencies. The inverse-Compton components of the SEDs have similar shapes as their synchrotron counterparts for all three cases.

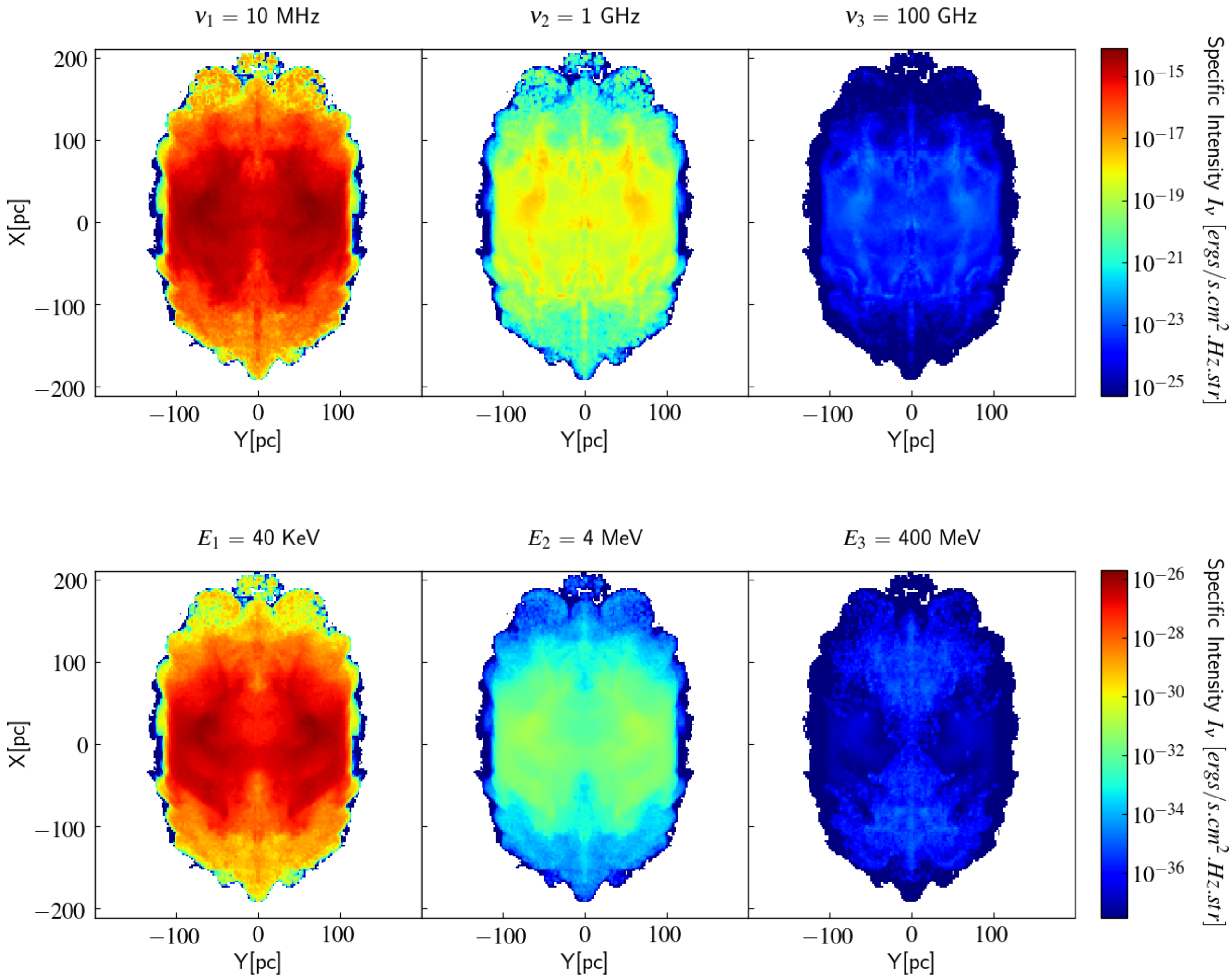

Figure 4.6: Top panel: Synchrotron emission maps produced using the hybrid framework in the PLUTO code for the UNI-B case at time t = 15.0 (in code units) for a direction along a line of sight inclined at 20° with the jet axis and initial spectral index of non-thermal particle distribution p = 6 at observing frequencies of 10MHz, 1GHz, and 100GHz. Bottom panel: Corresponding inverse-Compton emission maps at observing energies of 40KeV, 4MeV, and 400MeV with the other model parameters being the same.

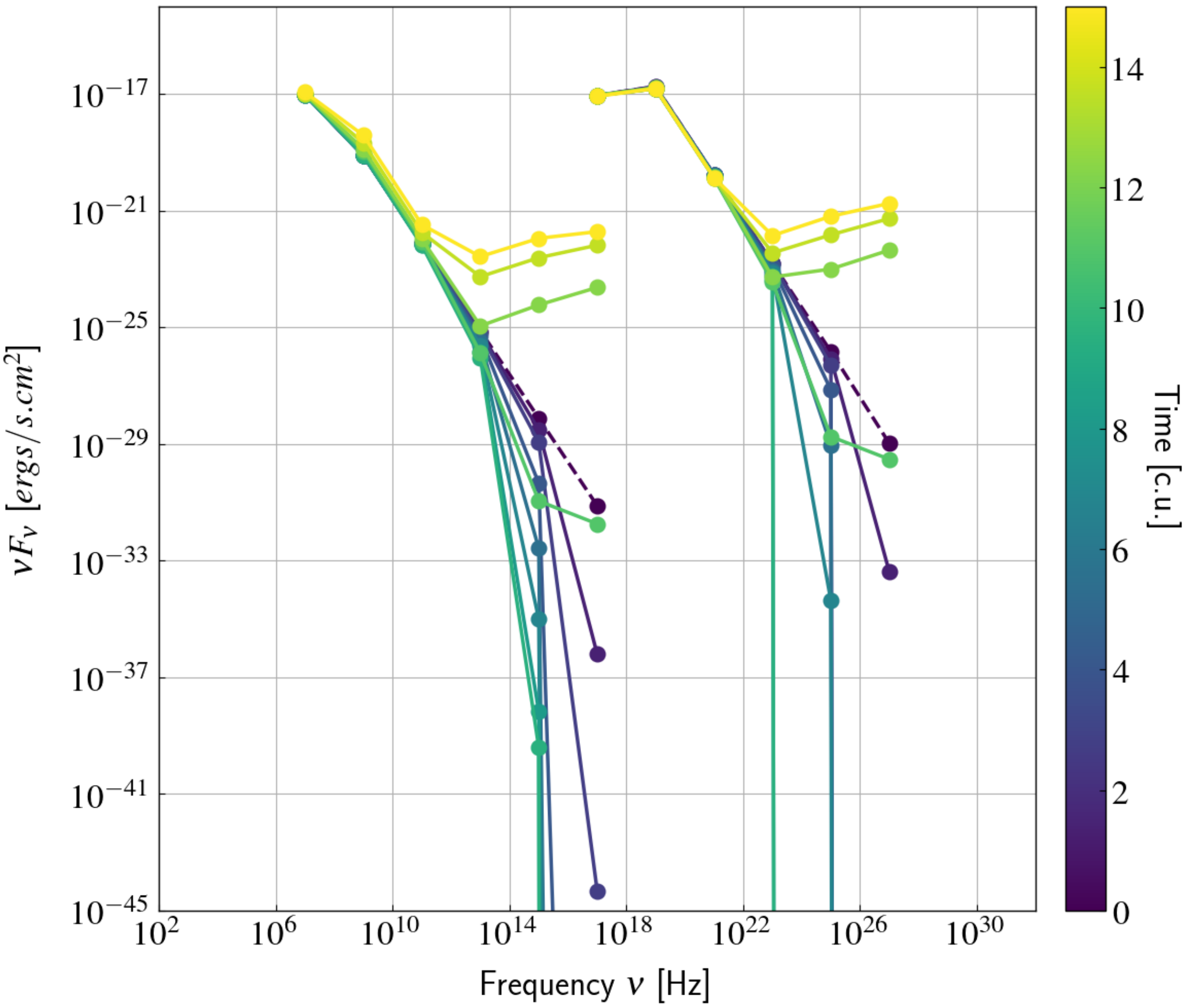

Figure 4.7: The time evolution of the SED for model UNI-B produced using the hybrid framework in the PLUTO code when observed from a direction inclined at 20° with the jet axis and the initial spectral index of the emitting electrons, p = 6. The colors represent incremental times starting from $t = 0.0$ to $t = 15.0$ in code units.

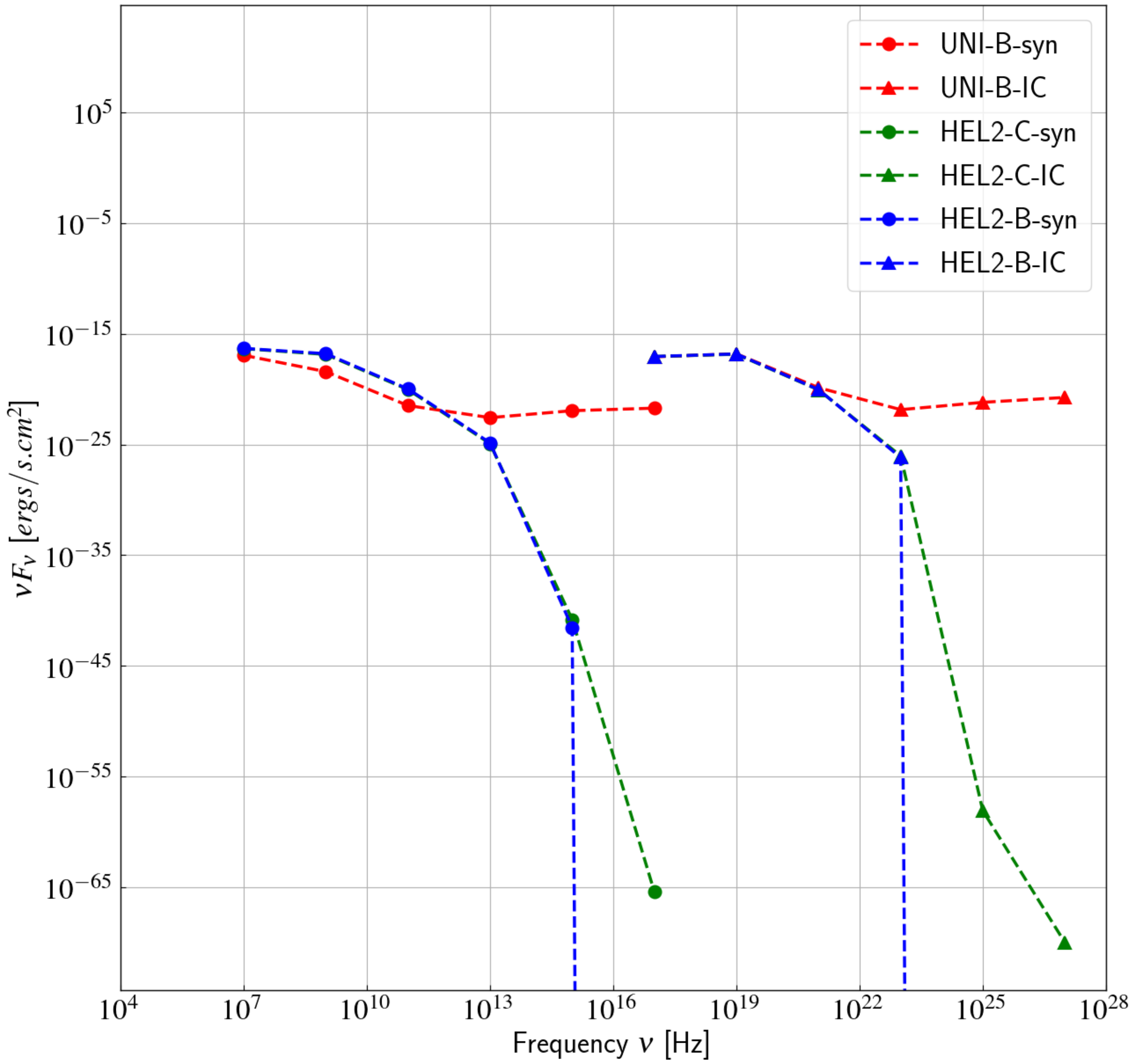

Figure 4.8: A comparison between the SED of cases UNI-B, HEL2-B, and HEL2-C produced using the hybrid framework in the PLUTO code at time $t = 15.0$ (in code units) for a direction along a line of sight inclined at 20° with the jet axis and the initial spectral index of the emitting electrons, p = 6.

Chapter 5

Discussion

The results of dynamical and emission modeling of magneto-hydrodynamic instabilities in jets have been described in Chapter 4. We now discuss the physical interpretation of the results obtained using dynamical modeling, while sections 5.2 and 5.3 are devoted to the discussion on results obtained from emission modeling.

5.1 Comparative overview

In the uniform magnetic field configurations UNI-A and UNI-B where the Kelvin-Helmholtz instability dominates, the jet gets completely destroyed by the time $t = 15.0$ in code units as compared to the helical magnetic field configurations HEL2-A and HEL2-B that have kink as well as Kelvin-Helmholtz instabilities in which the jet remains relatively stable. This has been shown through the three-dimensional temporal snapshots of the jet density structure given in Fig. 4.1. In the trans-sonic jet configuration UNI-A where the Kelvin-Helmholtz instability dominates, vortex growth occurs at the jet boundary (not shown). The magnetic field lines get concentrated around the edges of these vortices and the build-up of magnetic and kinetic energy E^b_{xy} and E^k_{xy}, in the transverse direction shown in Fig. 4.2 disrupts the flow whereas in the HEL2-A configuration, the vortex growth is suppressed by the azimuthal magnetic field B_ϕ which stabilizes the jet [6]. In the supersonic jet configurations, the instability starts developing when the axial kinetic energy E^k_z begins deviating from its initial value which occurs at $t = 13.5$ in code units in the UNI-B case and $t = 10.5$ in the HEL2-B case as shown in Fig. 4.2. In the UNI-B case, the Kelvin-Helmholtz instability makes the flow turbulent at small scales resulting in freshly formed shocks that disrupt the flow. Shock formation occurs at the jet boundary in proto-stellar outflows (see section 2.4 in [5]). In the HEL2-B case, the changes in the jet density occur at more secular scales (shown in Fig. 4.1) and the absence of shock formation at small scales thereof has a stabilizing effect on the jet.

5.2 Effects of viewing direction on jet emission

In this section, we first discuss the physical interpretation of the emission maps in Fig. 4.3 and Fig. 4.5 and the differences between them before diving into the effects of viewing direction $\hat{n}_{los}$ on the jet emission.

The initial distribution of non-thermal particles in all our emission models is a power-law given by equation 3.8. As a result, the number of non-thermal emitting electrons drops with energy which leads to a dimming effect in all of our emission maps with an increase in energy at the initial time. This is reflected in the synchrotron emission maps for the UNI-A case obtained at time $t = 9.0$ in code units shown in Fig. 4.3. Since these color maps are produced using the multi-zone model in which the non-thermal particle distribution does not vary with time or position in the grid, the emission maps exhibit this dimming effect at all times as is seen here at $t = 9.0$. The bright symmetric feature resembling a figure of eight which appears in these emission maps can be attributed to the magnetic field structure at $t = 9.0$. The Kelvin-Helmholtz instability in the UNI-A case leads to vortex formation at the jet boundary. The magnetic field lines get concentrated at the edges of the vortices due to a local increase in jet density which results in increased emission from these regions. The dimming effect is also visible in the synchrotron emission maps for the UNI-A case obtained using the hybrid framework in the PLUTO code at the same time as shown in Fig. 4.5. However, there is an enhanced dimming at higher energies as the bright feature almost vanishes in the emission map obtained at a frequency $\nu = 43$GHz. This difference is purely on the account of radiative losses as the UNI-A case does not show any shocks being trans-sonic. The non-thermal electrons lose energy with time due to the synchrotron cooling effect which results in the enhanced dimming of the jet emission at higher energies as the number of non-thermal electrons with higher energies will be lesser.

In section 4.2, we described the effects of the viewing direction $\hat{n}_{los}$ on the synchrotron emission spectra of all the jet configurations as shown in Fig. 4.4 at time $t = 9.0$ in code units. The results were obtained using a simplistic prescription of emission modeling- the multi-zone model which leads to small differences in the emission spectra of the jet. The total integrated flux levels in the uniform magnetic field configurations UNI-A and UNI-B are much lower than the helical magnetic field configurations for a direction along a line of sight closer to the axis ($\theta = 10°$) and are of the same order for a direction along a line of sight that is highly inclined with the jet axis ($\theta = 50°$). The increased synchrotron emission for the UNI-A and UNI-B cases at higher inclination angles of the line of sight with the jet axis can be attributed to the orientation of the line of sight vector $\hat{n}_{los}$ with the magnetic field vector $\vec{B}$ and the effect of particle acceleration caused by freshly formed shocks. We now discuss both of these reasons in detail.

1. **Effect of magnetic field orientation:** The synchrotron emissivity given by equation 3.2 goes directly as $|\vec{B} \times \hat{n}_{los}| \propto Bsin(\theta)$ where θ is the angle between the line of sight vector $\hat{n}_{los}$ and the magnetic field vector $\vec{B}$. In the uniform magnetic field configurations, the axial magnetic field dominates the transverse magnetic field in most of the grid zones. For a line of sight close to the jet axis ($\theta = 10°$), the contribution to the total integrated flux from most of the grid zones will be less as $sin(\theta)$ has smaller values for small θ. However, in the helical magnetic field configurations, the azimuthal magnetic field B_ϕ which is nearly perpendicular to a line of sight close to the jet axis, also contributes significantly to the synchrotron emission as $sin(\theta) \to 1$ for $\theta = 90°$. This explains the higher total integrated flux levels in the helical configurations for $\theta = 10°$. For $\theta = 50°$ on the other hand, the axial magnetic field in the uniform magnetic field configurations will now have a component that is perpendicular to the line of sight which contributes to the synchrotron emission of the jet. This results in the total integrated flux levels of the same order for all three configurations as shown in the right-hand panels of Fig. 4.4.

2. **Effect of particle acceleration due to shocks :** The convergence of density waves resulting in freshly formed shocks at small scales locally accelerates the non-thermal particles in the jet to higher energies. The particle acceleration leads to an increased emission at higher energies [13][2]. This is not apparent here as no shocks are detected in the supersonic jet configurations UNI-B and HEL2-B using the hybrid framework in PLUTO code until the time of comparison $t = 9.0$ in code units. The multi-zone model is a simplistic prescription of emission modeling in that it assumes that the initial power-law distribution of non-thermal particles does not change with time and thus fails to capture the effect of particle acceleration on the continuum emission spectra of the jet. It is still possible to compare the synchrotron spectra for the UNI-A and UNI-B cases obtained using the multi-zone model.In the UNI-B case, as the axial velocity is higher, the transverse kinetic and magnetic energies E^k_{xy} and E^b_{xy} do not build up rapidly at earlier times as is shown in Fig. 4.2 because it takes a long time for the Kelvin-Helmholtz instability to develop. While the transverse magnetic field is weak in the UNI-B case at time $t = 9.0$, the UNI-A case has relatively stronger magnetic fields in the transverse direction due to the vortices forming at the jet boundary as a result of the Kelvin-Helmholtz instability. Consequently, the synchrotron emission is lower in the UNI-B case as compared to the trans-sonic jet configuration UNI-A for $\theta = 10°$.

In the supersonic jet configuration UNI-B, both the synchrotron and IC emission maps obtained using the hybrid framework in the PLUTO code at time $t = 15.0$ in code units shown in Fig. 4.6 exhibit the dimming effect as in the UNI-A case. Also visible is an enhanced dimming at higher energies. This occurs due to the synchrotron cooling of non-thermal electrons that are responsible for the jet emission. The bright features appearing in the central region of the jet are a result of non-thermal particles getting locally accelerated to higher energies due to the convergence of density waves resulting in freshly formed shocks at small scales. The other way around, the jet emission can also be used to trace the shock structure in the jet.

5.3 Effects of MHD instabilities on jet emission

To study the effects of MHD instabilities on the jet emission, we described the temporal evolution of the continuum emission spectra for the supersonic jet configuration UNI-B in section 4.3. For the synchrotron emission, the total integrated flux at high frequencies of 10^{15}Hz in the optical waveband and 10^{17}Hz in the X-ray band drops progressively at times $t = 0.5, 1.0, 2.5, 4.5, 6.5, 9.0$, and 11.5 in code units as a result of synchrotron cooling of the non-thermal electrons. The Kelvin-Helmholtz instability makes the flow turbulent at small scales [11]. The MHD turbulence results in freshly formed shocks that are captured using the hybrid framework in the PLUTO code at time $t = 13.5$ in code units. The convergence of density waves which results in these shocks locally accelerates the non-thermal particles to higher energies thereby flattening the SED as a result of increased emission at high frequencies of 10^{15}Hz and 10^{17}Hz. γ-ray observations of the blazar Mrk 501 made by *Fermi*-LAT at times show similar flattening of the continuum emission spectra [21]. The inverse-Compton emission follows a similar trend of temporal evolution as it a result of CMB photons scattering off the same non-thermal electron population which is responsible for the synchrotron emission. After $t = 13.5$, when freshly formed shocks first appear, the number of shocked Lagrangian macro-particles grows rapidly with

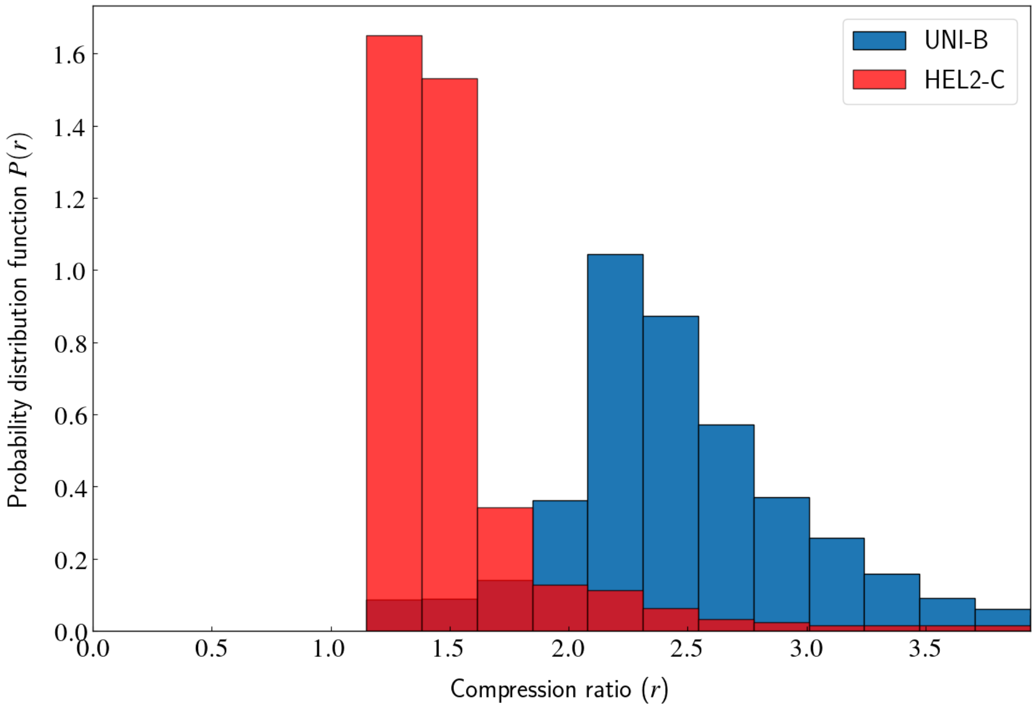

Figure 5.1: A histogram showing the probability density distribution of the number of macro-particles with compression ratio for the 'UNI-B' and 'HEL2-C' cases at time $t = 15.0$ in code units.

time. A histogram of the probability density distribution function $P(r)$ of these macro-particles with a compression ratio r is shown in Fig. 5.1 for the case UNI-B and the hypersonic jet configuration HEL2-C at time $t = 15.0$ in code units. The area under the histogram in each bin $P(r)\Delta r$ is the probability of a macro-particle having a compression ratio between r to $r + \Delta r$ where $\Delta r = 0.2$ is the bin width. We have about 5.5% and 8.3% particles in the UNI-B and HEL2-C cases respectively with a compression ratio $r > 4$ due to numerical artefacts and have been neglected in Fig. 5.1. The probability density distribution of macro-particles in the UNI-B case peaks at $r = 2.2$ indicating that the majority of the freshly formed shocks are moderately strong. In the helical jet configuration HEL2-C, the peak occurs at a compression ratio $r = 1.3$ indicating that the convergence of density waves is not focused enough to form shocks despite the high initial sonic Mach number $M_s = 5.0$ on the jet axis.

To interpret the effect of MHD instabilities on the jet emission, we described in section 4.3, a comparison between the spectra of the cases UNI-B, HEL2-B, and HEL2-C shown in Fig. 4.8 at time $t = 15.0$ in code units. In the UNI-B case, we see a flattening of the synchrotron component of the SED as the non-thermal electrons get locally accelerated to high energies due to the convergence of density waves resulting in freshly formed shocks at small scales arising from the turbulence-driven Kelvin-Helmholtz instability. As most of the shocked particles in the UNI-B case have a compression ratio $r = 2.2$, this results in a spectral index of $p = \frac{3r}{r-1} - 2 = 3.5$ for the ensemble of non-thermal electrons attached to these macro-particles according to Vaidya et al. [23]. Since the spectral energy density goes directly as $\nu F_\nu \propto \nu^{\frac{3-p}{2}}$, the net effect of these shocks is that the SED goes directly as $\nu^{-0.25}$ which flattens it. The flattening of the synchrotron SED according to this power-law with slope -0.25 is visible for frequencies ranging from 10^{11}Hz to 10^{13}Hz. The total integrated flux for higher frequencies between 10^{15}Hz and 10^{17}Hz increases as the shock accelerated non-thermal particles have not had sufficient time for the synchrotron cooling process to occur. In the helical magnetic configurations HEL2-B and HEL2-C, the synchrotron spectra are relatively steeper as the total integrated flux levels are much lower at high frequencies of 10^{15}Hz in the optical waveband and 10^{17}Hz in the X-ray band as the changes in jet density occur at more secular scales. This occurs either due to the absence of freshly forming shocks at small scales as in the HEL2-B case or the HEL2-C case where the convergence of density waves is not focused enough to form shocks despite ramping up the initial sonic Mach number to $M_s = 5.0$ on the jet axis. The synchrotron emission at a frequency of 10^{17}Hz in the X-ray band for the HEL2-C case is higher than that of the HEL2-B case despite there being no shocks as a result of the convergence of density waves in the HEL2-C case that is represented by the probability density distribution function $P(r)$ in the histogram in Fig. 5.1. As most of the shocked particles in the case HEL2-C have a compression ratio $r = 1.3$, we get $p = \frac{3r}{r-1} - 2 = 11$ for these particles and the SED goes directly as $\nu^{\frac{3-p}{2}} = \nu^{-4}$ making the spectrum steep. The slope of the synchrotron component of the SED in the frequency range between 10^{11}Hz to 10^{13}Hz is nearest to -4. The total integrated flux for higher frequencies between 10^{15}Hz and 10^{17}Hz drops as a result of synchrotron cooling. The corresponding inverse-Compton components of the spectra have similar shapes as the same electron population is responsible for both synchrotron and inverse-Compton emission.

In conclusion, the jet configuration dominated by the Kelvin-Helmholtz instability has disruptive flow causing shock formation which results in a flatter emission spectrum while the jet configuration that has both kink and Kelvin-Helmholtz instabilities is relatively stable with no shocks leading to a steeper emission spectrum.

Chapter 6

Summary and Outlook

Using dynamical modeling, we have studied the effects of MHD instabilities on jet dynamics and energetics that have implications for jet stability at scales of hundreds of kilo-parsecs. Note that the high-resolution hydrodynamic simulations conducted by Bodo et al. [8] could not reproduce coherent jets at these scales as revealed by observations. In order to validate our dynamical models, we studied the energetics of three trans-sonic jet configurations UNI-A, HEL1-A, and HEL2-A and our results shown in Fig. 4.2 are in agreement with those obtained by Baty and Keppens [6] for all three models with the same initial conditions. The uniform magnetic field configurations UNI-A and UNI-B exhibit disruptive flow whereas the helical magnetic field configurations HEL2-A and HEL2-B are relatively stable as shown in Fig. 4.1.

Having studied the jet dynamics and energetics, we do the emission modeling to study the effect of MHD instabilities on the continuum emission spectra of the jet. We have developed a simplistic prescription to achieve this - the multi-zone model. We validate a limiting case of this - the one-zone model by comparing results obtained using the NAIMA code for the same set of model parameters [12]. However, in order to capture localized physical effects such as shocks, a more accurate emission model is required - the hybrid macro-particle based model. We use this model through the hybrid framework in the PLUTO code. The synchrotron emission maps for the UNI-A case obtained using the multi-zone model shown in Fig. 4.3 have been compared with those obtained using the hybrid macro-particle based model shown in Fig. 4.5. An enhanced dimming is seen in the emission maps shown in Fig. 4.5 at higher energies. This difference is purely on the account of synchrotron cooling of the non-thermal electrons as the UNI-A case does not show any shocks being trans-sonic.

Using the multi-zone model, we have studied the effect that the orientation of the magnetic field vector $\vec{B}$ with the line of sight vector $\hat{n}_{los}$ has on the synchrotron emission of the jet. As the synchrotron emissivity goes directly as $|\vec{B} \times \hat{n}_{los}| = Bsin\theta$, the total integrated flux levels rise with an increase in the inclination θ of the line of sight with the jet axis in the uniform magnetic field configuration.

The effect of MHD instabilities on the continuum emission spectra of the jet has been investigated using the hybrid framework in the PLUTO code. In the supersonic jet configuration with a uniform magnetic field UNI-B, we see a flattening of the SED due to localized physical effects such as particle acceleration caused by the convergence of density waves resulting in freshly formed shocks at small scales arising from the turbulence driven Kelvin-Helmholtz instability. In the helical magnetic field configuration HEL2-B which also has the kink instability, the SED is relatively steeper at higher energies as the changes in jet density occur at secular scales. To summarise, if the Kelvin-Helmholtz instability dominates, it disrupts the flow causing shock formation which results in a flatter emission spectrum whereas the interaction between the kink and Kelvin-Helmholtz instabilities has a stabilizing effect on the jet making the emission spectra steep.

Having studied the emission properties of jets and their dependence on MHD instabilities, we are now in a position to explore the polarization aspect of the jet emission with the aid of observations made by upcoming projects such as the Imaging X-ray Polarimetry Explorer (IXPE) and the enhanced X-ray Timing and Polarimetry mission (eXTP). By studying the polarization properties of the jet emission, we can probe into the magnetic field structure of the jet [4]. We aim to pursue this in future work.

Bibliography

[1] F. A. Aharonian, S. R. Kelner, and A. Yu. Prosekin. Angular, spectral, and time distributions of highest energy protons and associated secondary gamma rays and neutrinos propagating through extragalactic magnetic and radiation fields. , 82(4):043002, August 2010.

[2] M. L. Ahnen, S. Ansoldi, L. A. Antonelli, C. Arcaro, A. Babić, B. Banerjee, P. Bangale, U. Barres de Almeida, J. A. Barrio, J. Becerra González, W. Bednarek, E. Bernardini, A. Berti, W. Bhattacharyya, O. Blanch, G. Bonnoli, R. Carosi, A. Carosi, A. Chatterjee, S. M. Colak, P. Colin, E. Colombo, J. L. Contreras, J. Cortina, S. Covino, P. Cumani, P. Da Vela, F. Dazzi, A. De Angelis, B. De Lotto, M. Delfino, J. Delgado, F. Di Pierro, M. Doert, A. Domínguez, D. Dominis Prester, M. Doro, D. Eisenacher lawion, M. Engelkemeier, V. Fallah Ramazani, A. Fernández-Barral, D. Fidalgo, M. V. Fonseca, L. Font, C. Fruck, D. Galindo, R. J. García López, M. Garczarczyk, M. Gaug, P. Giammaria, N. Godinović, D. Gora, D. Guberman, D. Hadasch, A. Hahn, T. Hassan, M. Hayashida, J. Herrera, J. Hose, D. Hrupec, K. Ishio, Y. Konno, H. Kubo, J. Kushida, D. Kuveždić, D. Lelas, E. Lindfors, S. Lombardi, F. Longo, M. López, C. Maggio, P. Majumdar, M. Makariev, G. Maneva, M. Manganaro, L. Maraschi, M. Mariotti, M. Martínez, D. Mazin, U. Menzel, M. Minev, J. M. Miranda, R. Mirzoyan, A. Moralejo, V. Moreno, E. Moretti, T. Nagayoshi, V. Neustroev, A. Niedzwiecki, M. Nievas Rosillo, C. Nigro, K. Nilsson, D. Ninci, K. Nishijima, K. Noda, L. Nogués, S. Paiano, J. Palacio, D. Paneque, R. Paoletti, J. M. Paredes, G. Pedaletti, M. Peresano, L. Perri, M. Persic, P. G. Prada Moroni, E. Prand ini, I. Puljak, J. R. Garcia, I. Reichardt, M. Ribó, J. Rico, C. Righi, A. Rugliancich, T. Saito, K. Satalecka, S. Schroeder, T. Schweizer, S. N. Shore, J. Sitarek, I. Šnidarić, D. Sobczynska, A. Stamerra, M. Strzys, T. Surić, L. Takalo, F. Tavecchio, P. Temnikov, T. Terzić, M. Teshima, N. Torres-Albà, A. Treves, S. Tsujimoto, G. Vanzo, M. Vazquez Acosta, I. Vovk, J. E. Ward, M. Will, D. Zarić, A. Arbet-Engels, D. Baack, M. Balbo, A. Biland, M. Blank, T. Bretz, K. Bruegge, M. Bulinski, J. Buss, A. Dmytriiev, D. Dorner, S. Einecke, D. Elsaesser, T. Herbst, D. Hildebrand, L. Kortmann, L. Linhoff, M. Mahlke, K. Mannheim, S. A. Mueller, D. Neise, A. Neronov, M. Noethe, J. Oberkirch, A. Paravac, W. Rhode, B. Schleicher, F. Schulz, K. Sedlaczek, A. Shukla, V. Sliusar, R. Walter, A. Archer, W. Benbow, R. Bird, R. Brose, J. H. Buckley, V. Bugaev, J. L. Christiansen, W. Cui, M. K. Daniel, A. Falcone, Q. Feng, J. P. Finley, G. H. Gilland ers, O. Gueta, D. Hanna, O. Hervet, J. Holder, G. Hughes, M. Hütten, T. B. Humensky, C. A. Johnson, P. Kaaret, P. Kar, N. Kelley-Hoskins, M. Kertzman, D. Kieda, M. Krause, F. Krennrich, S. Kumar, M. J. Lang, T. T. Y. Lin, G. Maier, S. McArthur, P. Moriarty, R. Mukherjee, S. O'Brien, R. A. Ong, A. N. Otte, N. Park, A. Petrashyk, A. Pichel, M. Pohl, J. Quinn, K. Ragan, P. T. Reynolds, G. T. Richards, E. Roache,

A. C. Rovero, C. Rulten, I. Sadeh, M. Santander, G. H. Sembroski, K. Shahinyan, I. Sushch, J. Tyler, S. P. Wakely, A. Weinstein, R. M. Wells, P. Wilcox, A. Wilhel, D. A. Williams, T. J Williamson, B. Zitzer, M. Perri, F. Verrecchia, C. Leto, M. Villata, C. M. Raiteri, S. G. Jorstad, V. M. Larionov, D. A. Blinov, T. S. Grishina, E. N. Kopatskaya, E. G. Larionova, A. A. Nikiforova, D. A. Morozova, Yu. V. Troitskaya, I. S. Troitsky, O. M. Kurtanidze, M. G. Nikolashvili, S. O. Kurtanidze, G. N. Kimeridze, R. A. Chigladze, A. Strigachev, A. C. Sadun, J. W. Moody, W. P. Chen, H. C. Lin, J. A. Acosta-Pulido, M. J. Arévalo, M. I. Carnerero, P. A. González-Morales, A. Manilla-Robles, H. Jermak, I. Steele, C. Mundell, E. Benítez, D. Hiriart, P. S. Smith, W. Max-Moerbeck, A. C. S. Readhead, J. L. Richards, T. Hovatta, A. Lähteenmäki, M. Tornikoski, J. Tammi, M. Georganopoulos, and M. G. Baring. Extreme HBL behavior of Markarian 501 during 2012. , 620:A181, December 2018.

[3] S. Appl, T. Lery, and H. Baty. Current-driven instabilities in astrophysical jets. Linear analysis. , 355:818–828, March 2000.

[4] Sayali S. Avachat, Eric S. Perlman, Steven C. Adams, Mihai Cara, Frazer Owen, William B. Sparks, and Markos Georganopoulos. Multi-wavelength Polarimetry and Spectral Study of the M87 Jet During 2002-2008. , 832(1):3, November 2016.

[5] John Bally. Protostellar outflows. *Annual Review of Astronomy and Astrophysics*, 54(1):491–528, 2016.

[6] H. Baty and R. Keppens. Interplay between Kelvin-Helmholtz and Current-driven Instabilities in Jets. , 580(2):800–814, Dec 2002.

[7] George R. Blumenthal and Robert J. Gould. Bremsstrahlung, Synchrotron Radiation, and Compton Scattering of High-Energy Electrons Traversing Dilute Gases. *Reviews of Modern Physics*, 42(2):237–271, January 1970.

[8] G. Bodo, P. Rossi, S. Massaglia, A. Ferrari, A. Malagoli, and R. Rosner. Three-dimensional simulations of jets. , 333:1117–1129, May 1998.

[9] Peter Breiding, Eileen T. Meyer, Markos Georganopoulos, M. E. Keenan, N. S. DeNigris, and Jennifer Hewitt. Fermi Non-detections of Four X-Ray Jet Sources and Implications for the IC/CMB Mechanism. , 849(2):95, November 2017.

[10] Carl-Gunne Fälthammar. Arnab rai choudhuri, the physics of fluids and plasmas: An introduction for astrophysicists. *Space Science Reviews*, 88(3):613–614, Apr 1999.

[11] E. Kersalé, P. Y. Longaretti, and G. Pelletier. Pressure- and magnetic shear-driven instabilities in rotating MHD jets. , 363:1166–1176, November 2000.

[12] D. Khangulyan, F. A. Aharonian, and S. R. Kelner. Simple Analytical Approximations for Treatment of Inverse Compton Scattering of Relativistic Electrons in the Blackbody Radiation Field. , 783(2):100, March 2014.

[13] MAGIC Collaboration, V. A. Acciari, S. Ansoldi, L. A. Antonelli, A. Babić, B. Banerjee, U. Barres de Almeida, J. A. Barrio, J. Becerra González, W. Bednarek, E. Bernardini, A. Berti, J. Besenrieder, W. Bhattacharyya, C. Bigongiari, O. Blanch, G. Bonnoli, G. Busetto, R. Carosi, G. Ceribella, S. Cikota, S. M. Colak, P. Colin, E. Colombo, J. L. Contreras, J. Cortina, S. Covino, V. D'Elia, P. da Vela, F. Dazzi,

A. de Angelis, B. de Lotto, M. Delfino, J. Delgado, F. di Pierro, E. Do Souto Espiñera, A. Domínguez, D. Dominis Prester, M. Doro, V. Fallah Ramazani, A. Fattorini, A. Fernández-Barral, G. Ferrara, D. Fidalgo, L. Foffano, M. V. Fonseca, L. Font, C. Fruck, D. Galindo, S. Gallozzi, R. J. García López, M. Garczarczyk, S. Gasparyan, M. Gaug, P. Giammaria, N. Godinović, D. Guberman, D. Hadasch, A. Hahn, T. Hassan, J. Herrera, J. Hoang, D. Hrupec, S. Inoue, K. Ishio, Y. Iwamura, H. Kubo, J. Kushida, D. Kuveždić, A. Lamastra, D. Lelas, F. Leone, E. Lindfors, S. Lombardi, F. Longo, M. López, A. López-Oramas, B. Machado de Oliveira Fraga, C. Maggio, P. Majumdar, M. Makariev, M. Mallamaci, G. Maneva, M. Manganaro, L. Maraschi, M. Mariotti, M. Martínez, S. Masuda, D. Mazin, M. Minev, J. M. Miranda, R. Mirzoyan, E. Molina, A. Moralejo, V. Moreno, E. Moretti, P. Munar-Adrover, V. Neustroev, A. Niedzwiecki, M. Nievas Rosillo, C. Nigro, K. Nilsson, D. Ninci, K. Nishijima, K. Noda, L. Nogués, S. Paiano, J. Palacio, D. Paneque, R. Paoletti, J. M. Paredes, G. Pedaletti, P. Peñil, M. Peresano, M. Persic, P. G. Prada Moroni, E. Prand ini, I. Puljak, J. R. Garcia, M. Ribó, J. Rico, C. Righi, A. Rugliancich, L. Saha, N. Sahakyan, T. Saito, K. Satalecka, T. Schweizer, J. Sitarek, I. Šnidarić, D. Sobczynska, A. Somero, A. Stamerra, M. Strzys, T. Surić, F. Tavecchio, P. Temnikov, T. Terzić, M. Teshima, N. Torres-Albà, S. Tsujimoto, J. van Scherpenberg, G. Vanzo, M. Vazquez Acosta, I. Vovk, M. Will, D. Zarić, Fact Collaboration, A. Arbet-Engels, D. Baack, M. Balbo, A. Biland, M. Blank, T. Bretz, K. Bruegge, M. Bulinski, J. Buss, M. Doerr, D. Dorner, S. Einecke, D. Elsaesser, D. Hildebrand, L. Linhoff, K. Mannheim, S. Mueller, D. Neise, A. Neronov, M. Noethe, A. Paravac, W. Rhode, B. Schleicher, F. Schulz, K. Sedlaczek, A. Shukla, V. Sliusar, E. von Willert, R. Walter, C. Wendel, A. Tramacere, A. Lien, M. Perri, F. Verrecchia, M. Armas Padilla, C. Leto, A. Lähteenmäki, M. Tornikoski, and J. Tammi. Study of the variable broadband emission of Markarian 501 during the most extreme Swift X-ray activity. , 637:A86, May 2020.

[14] A. Mignone, G. Bodo, S. Massaglia, T. Matsakos, O. Tesileanu, C. Zanni, and A. Ferrari. PLUTO: A Numerical Code for Computational Astrophysics. , 170(1):228–242, May 2007.

[15] Alex Pandya, Zhaowei Zhang, Mani Chandra, and Charles F. Gammie. Polarized Synchrotron Emissivities and Absorptivities for Relativistic Thermal, Power-law, and Kappa Distribution Functions. , 822(1):34, May 2016.

[16] O. Petruk. Approximation of the radiation power of electrons due to the inverse-Compton process in the black-body photon field. , 499(3):643–648, June 2009.

[17] Oliver Porth, Christian Fendt, Zakaria Meliani, and Bhargav Vaidya. Synchrotron Radiation of Self-collimating Relativistic Magnetohydrodynamic Jets. , 737(1):42, August 2011.

[18] Stefan Reissl, Robert Brauer, Ralf S. Klessen, and Eric W. Pellegrini. Radiative Transfer with POLARIS. II. Modeling of Synthetic Galactic Synchrotron Observations. , 885(1):15, November 2019.

[19] S. Sahayanathan and S. Godambe. Modelling the very high energy flare of 3C 279 using one-zone leptonic model. , 419(2):1660–1666, January 2012.

[20] R. Schlickeiser and J. Ruppel. Klein-Nishina steps in the energy spectrum of galactic cosmic-ray electrons. *New Journal of Physics*, 12(3):033044, March 2010.

[21] A. Shukla, K. Mannheim, V. R. Chitnis, J. Roy, B. S. Acharya, D. Dorner, G. Hughes, and A. Biland. Detection of Very Hard γ-Ray Spectrum from the TeV Blazar Mrk 501. , 832(2):177, December 2016.

[22] Helmut Steinle. Centaurus A: A Multifrequency Review. *Chinese Journal of Astronomy and Astrophysics Supplement*, 6(S1):106–113, December 2006.

[23] Bhargav Vaidya, Andrea Mignone, Gianluigi Bodo, Paola Rossi, and Silvano Massaglia. A Particle Module for the PLUTO Code. II. Hybrid Framework for Modeling Nonthermal Emission from Relativistic Magnetized Flows. , 865(2):144, October 2018.

[24] V. Zabalza. Naima: a Python package for inference of particle distribution properties from nonthermal spectra. In *34th International Cosmic Ray Conference (ICRC2015)*, volume 34 of *International Cosmic Ray Conference*, page 922, July 2015.